STUDIES OF ANTINEUTRINOS AT NUCLEAR REACTORS

and

ATOMIC FINAL STATE EFFECTS IN TESTS OF T-VIOLATION

Thesis by
Brian R. Davis

In Partial Fulfillment of the Requirements
for the Degree of
Doctor of Philosophy

California Institute of Technology
Pasadena, California

1980

(Submitted May 9, 1980)

ACKNOWLEDGMENTS

I am very grateful to Drs. Felix Boehm, William Fowler, Steven Koonin, and Petr Vogel for the direction provided me during these years at CalTech. The quality of their scientific work has challenged me in my education as a physicist, and each has greatly assisted me in this development.

For their help in the preparation of this thesis, I wish to especially thank Mrs. Elsa Garcia, Mr. Mike McNab, and Dr. Klaus Lackner.

It is a special joy for me to walk in fellowship with the men and women of Saddleback Covenant Church. I am deeply appreciative of their support and prayers. The life which we share is that of the Lord Jesus, who calls man from the way of deception to seek His way of truth and hope.

I cherish the closeness which I enjoy with the members of my family : my sister Christine; my sister-in-law Nancy, brother Michael, and niece Meghan; and my mother and father. Their encouragement and love toward me has been constant, and I have been strengthened through their prayers on my behalf.

I dedicate this thesis to my parents, for raising me in the nurture and admonition of the Lord.

ABSTRACT

Part I. Nuclear reactors, due to their large flux of low energy electron antineutrinos, are profitable locations for studies of antineutrino induced reactions and possible neutrino oscillations. The calculation of the reactor antineutrino spectrum is presented, together with predictions for weak-interaction experiments performed at nuclear reactors. It is demonstrated that such experiments provide constraints on the parameters describing neutrino oscillations.

Part II. Due to interference of atomic processes with nuclear electromagnetic transitions, the emitted radiation acquires a phase shift. The knowledge of accurate values for this phase shift, also called the interference parameter, must be included in the analysis of time-reversal and Mössbauer absorption experiments. Theoretical expressions for the interference parameter are presented, and calculated values are compared with experiment. Satisfactory agreement is obtained. In particular, an apparent violation of time-reversal invariance in the 129 keV transition of ^{191}Ir is fully explained by these atomic interference effects.

TABLE OF CONTENTS

PART I

STUDIES OF ANTINEUTRINOS AT NUCLEAR REACTORS

CHAPTER 1

SEARCHES FOR NEUTRINO OSCILLATIONS AT NUCLEAR REACTORS

SEARCHES FOR NEUTRINO OSCILLATIONS AT NUCLEAR REACTORS

1. INTRODUCTION

In recent years, there has been substantial theoretical speculation concerning the possible non-conservation of individual lepton numbers. A violation of this type could manifest itself in several ways, one of which is the possible decay of the muon into an electron and photon. It has been suggested that another consequence might be the existence of oscillations between neutrinos of the electron, muon, and tau varieties. Experiments have been designed to search for this possibility at various locations, including high energy accelerators, intermediate energy meson factories, and nuclear reactors. A thorough review of both theory and experiment may be found in Ref. 1.

Nuclear reactors, due to their large flux of low energy antineutrinos, are profitable locations for studies of antineutrino induced reactions and possible neutrino oscillations. The calculation of the antineutrino spectrum presented in Chapter 2 was primarily motivated by an experimental search for oscillations by a Caltech-Munich-Grenoble collaboration.[2] This experiment is presently being conducted at a research reactor located at the Laue-Langevin Institute in Grenoble, France. Reactor experiments have also been performed and are being continued at the Savannah River, South Carolina location by Reines and his collaborators.[3-5] If these experiments are not successful in actually observing neutrino oscillations, they will nevertheless provide valuable constraints on the parameters involved.

In this chapter we first discuss a phenomenological model for oscillations between neutrinos of different flavors. Mixing of only two neutrino types will be described, although the analysis can be easily generalized to include more flavors. We then consider the possible consequences of neutrino oscillations for nuclear reactor experiments. It will be demonstrated that various experimental results may be used together to determine or limit the oscillation parameters.

2. MODEL FOR NEUTRINO OSCILLATIONS

There have been in the past 25 years several suggestions for possible physical transformations between neutrino types. These have included oscillations between neutrinos and their antiparticles, and the decay of one neutrino type into another type with the emission of a third particle. Recent theoretical discussion has also concerned the possible mixing of neutrinos from various families. Today the families include those of the electron, muon, and tau with the possibility of additional families. The existing experimental data on the properties of these neutrinos hardly restrict their masses to be zero, an assumption widely employed in the past.

The phenomenon of mixing between particles is known from both the neutral kaon and quark systems. Mixing results from the total Hamiltonian containing two parts, one part violating the quantum numbers conserved by the other. For the case of quarks, the weak eigen-states, d' and s', are orthogonal combinations of the strong eigen-states, d and s, with the mixing characterized by the Cabibbo angle. For the neutral kaon system, the strong eigen-states, K° and $\bar{K}^\circ$, are superpositions of the weak eigen-states, K_L, and K_S. Because the K_L and K_S

have slightly different masses, their time development is determined by different frequencies. This results in transformations between the K° and its antiparticle, the $\bar{K}^\circ$.

Extending these examples to the case of neutrinos, we assume that the neutrino eigenstates of the weak interaction (ν_e, ν_μ, ν_τ...) are orthogonal combinations of the mass eigenstates (ν_1, ν_2, ν_3...). The following discussion, which also applies to the antineutrinos is similar to that of Mann and Primakoff.[6] We consider explicitly the case of two neutrinos, ν_e and ν_α, writing them as linear combinations of ν_1 and ν_2:

$$\begin{pmatrix} \nu_e \\ \nu_\alpha \end{pmatrix} = \begin{pmatrix} \cos\theta & \sin\theta \\ -\sin\theta & \cos\theta \end{pmatrix} \begin{pmatrix} \nu_1 \\ \nu_2 \end{pmatrix} \quad . \tag{1}$$

Requiring K° and $\bar{K}^\circ$ to be CP eigen-states necessarily fixes the mixing angle in the neutral kaon system at 45°. However, for neutrinos, as is the case for quarks, there is no strong compelling reason at the present time to prefer a specific value for the angle of mixing. It remains a parameter of the oscillation to be determined.

A beam of electron type neutrinos of momentum $\underline{p}$ produced via the weak interaction will, provided the following conditions are met, oscillate into the other variety "α":

1) the mixing angle is non-zero ($\theta \neq 0$)

2) the masses of the mass eigen-states are unequal ($m_1 \neq m_2$). The probability $P(\nu_e, d)$ of observing an electron type neutrino at distance d away from the source can be shown to equal:

$$P(\nu_e,d) = P(\nu_e,d=0) \left\{1 - \frac{1}{2} \sin^2 2\theta \left(1 - \cos\left[\frac{(E_2 - E_1)d}{\hbar c}\right]\right)\right\} . \quad (2)$$

where

$$E_i = \sqrt{p^2c^2 + m_i^2c^4} \quad (3a)$$

$$\approx pc + \frac{m_i^2 c^3}{2p} . \quad (3b)$$

Equation (3b) is valid for $pc >> m_ic^2$ which is likely satisfied at reactor neutrino energies of a few MeV.

One is then able to rewrite Eq. (2) as:

$$P(\nu_e,d) = P(\nu_e,d=0) \left\{1 - \frac{1}{2} \sin^2 2\theta \left(1 - \cos\left[\frac{2.54\ \Delta^2 d}{E_\nu}\right]\right)\right\} , \quad (4)$$

where $\Delta^2 = (m_2^2 - m_1^2)c^4$ is measured in eV^2, d is measured in meters, and E_ν is the energy of the original neutrino measured in MeV.

The difference of the squared masses, Δ^2, is the second parameter necessary for the description of oscillations. The sensitivity with which it can be determined in an experimental search for oscillations is determined by the neutrino energy and the distance between source and detector. That is, a rough estimate of the minimum value of Δ^2 observable in a given experiment can be obtained by setting the argument of the cosine equal to 2π:

$$\Delta^2_{min} \approx \frac{2.5\ E_\nu}{d} . \quad (5)$$

Δ^2_{min} is again given in eV^2 when E_ν is measured in MeV and d in meters. Δ^2_{min} is $\sim 3 \times 10^{-2}$ for reactors and $\sim 3 \times 10^{-1}$ for meson

factories and high-energy accelerators.[1]

Therefore, two parameters are required for the description of mixing between two neutrinos: $\sin^2 2\theta$ is the amplitude of the oscillation, and Δ^2 gives the dependence upon distance and neutrino energy. The present experimental limits on neutrino oscillations can be simply expressed in terms of Δ^2, if maximal mixing ($\theta = 45°$) is assumed. The analysis[1] of the Nezrick and Reines[4] inverse neutron decay measurement yields $\Delta^2 \lesssim 1\ eV^2$ for $\bar{\nu}_e \rightarrow$ anything. Results of the Gargamelle collaboration[7] on $\nu_\mu \rightarrow \nu_e$ and $\bar{\nu}_\mu \rightarrow \bar{\nu}_e$ also limit $\Delta^2 \lesssim 1\ eV^2$. Recent analysis of a Los Alamos experiment[8] constrains $\Delta^2 \lesssim .64\ eV^2$ for the oscillation channel $\bar{\nu}_\mu \rightarrow \bar{\nu}_e$.

3. EXPERIMENTAL CONSEQUENCES OF OSCILLATIONS FOR REACTOR EXPERIMENTS

The sensitivity of reactor experiments to small values of Δ^2 makes them particularly attractive for neutrino oscillation searches. Reactor searches are also very desirable because they look for the transformation of $\bar{\nu}_e$ into anything else, and are therefore not limited to observing a specific product of the oscillation.

As is clear from Eq. (4), the existence of oscillations will cause the spectrum of antineutrinos produced at a reactor to change shape as a function of distance from the source. If the core dimensions are small relative to d, we may employ this expression to generate Fig. 1 showing the change in spectral shape for specific values of Δ^2 and θ. The spectrum of $\bar{\nu}_e$'s at distance d from the reactor is $n(E_{\bar{\nu}}) \cdot P(E_{\bar{\nu}}, d)$, where $n(E_{\bar{\nu}})$ is the spectrum in the absence of oscillations.

In Sect. 4 of Chapter 2 the four antineutrino induced reactions conducted at nuclear reactors are discussed in detail. Here we only

consider the effect of possible neutrino oscillations upon these measurements, and show how the experimental results may, in principle, be used to constrain the parameters Δ^2 and θ.

Inverse Neutron Decay ($\bar{\nu}_e + p \rightarrow n + e^+$)

Only electron type antineutrinos are capable of producing the positrons observed in this reaction. The existence of oscillations would modify the expected yield of positrons $Y(E_{e^+}, d)$ of kinetic energy E_{e^+} at distance d:

$$Y(E_{e^+}, d) = n(E_{\bar{\nu}}) \; P(E_{\bar{\nu}}, d) \; \sigma(E_{\bar{\nu}}), \tag{6}$$

where $\sigma(E_{\bar{\nu}})$ is the cross section for monoenergetic antineutrinos, and $E_{e^+} = E_{\bar{\nu}} - 1.8$ MeV. In Figure 2 the affect of oscillations upon the expected positron spectrum is shown. The values of Δ^2, θ, and d were chosen identical to those of Figure 1.

If one assumes that the reactor $\bar{\nu}_e$ spectrum is known, then it is possible to exclude certain regions in the Δ^2, θ plane by comparison with measured positron spectra. In Figure 3, a χ^2 test of agreement between oscillated spectra and a hypothetically measured e^+ spectrum demonstrates how the parameters Δ^2 and $\sin^2 2\theta$ may be constrained. One difficulty with this procedure is its dependence upon the assumed $\bar{\nu}_e$ spectrum, yielding quite different results for the Davis-Vogel[9] and Avignone[10] spectra. This can perhaps be remedied by measurements of the positron spectrum at two distances; a departure of the total cross section from the expected $\frac{1}{r^2}$ dependence would, at the least, demonstrate the existence of oscillations. Further experimental studies of this reaction

by the Caltech-Munich-Grenoble and Irvine groups are now in progress.

Charged and Neutral Current Deuteron Disintegration $(\bar{\nu}_e + d \rightarrow n + n + e^+)$ $(\bar{\nu}_e + d \rightarrow n + p + \bar{\nu}_e)$

Since the publication of our paper on reactor antineutrino spectra,[9] Pasierb *et al.*[5] have observed the weak neutral and charged current deuteron disintegrations. The measured cross sections, expressed at ratios to our predictions in Table 1 of Chapter 2, are 0.8 ± 0.2 (neutral current) and 0.7 ± 0.2 (charged current). The respective ratios for the Avignone spectrum[11] are 0.55 ± 0.1 (neutral current) and 0.4 ± 0.1 (charged current).

The charged current deuteron disintegration depends upon the electron character of the incoming antineutrino. In contrast, the neutral current disintegration is assumed to be insensitive to neutrino oscillations between families. That is, even if the $\bar{\nu}_e$ changes into either $\bar{\nu}_\mu$ or $\bar{\nu}_\tau$, the standard Weinberg-Salam model predicts the neutral current couplings for all three antineutrinos to be equal. It is possible to use each of these deuteron experiments to test the existence of oscillations as was done for the inverse neutron decay. However, the conclusions drawn from such an analysis severely depend upon the theoretical $\bar{\nu}_e$ spectrum employed. (We note that it is disturbing that Avignone's neutral current ratio is so far from the value of one, expected even in the event of oscillations).

It has been noticed by Reines and his collaborators[12] that the sensitivity of such an analysis to the antineutrino spectrum can be substantially reduced by considering the following ratio:

$$R = \frac{\sigma^{c.c.}(exp)}{\sigma^{c.c.}(theor)} \Big/ \frac{\sigma^{n.c.}(exp)}{\sigma^{n.c.}(theor)} \quad . \tag{7}$$

Based on the experimental results of Ref. 5, we obtain $R = 0.9 \pm 0.3$ for the Davis-Vogel spectrum, and $R = 0.75 \pm 0.2$ for Avignone.[11] A determination of which values of Δ^2, θ are consistent with specific values for R yields constraints such as those shown in Figure 4. The shaded region indicates the oscillation parameters allowable for R between 0.6 and 0.9. The Davis-Vogel spectrum was employed for this comparison although similar results are obtained with other $\bar{\nu}_e$ spectra.

Antineutrino-Electron Scattering ($\bar{\nu}_e + e^- \rightarrow \bar{\nu}_e + e^-$)

For incident electron type antineutrinos, this reaction has contributions from both the charged and neutral current portions of the weak interaction. A comparison of theory with experiment permits determination of the Weinberg angle θ_w.[3] If mixing occurs, the product of the oscillation interacts only via the neutral current. This modifies the cross section for the production of electrons of kinetic energy T to be:

$$\frac{d\sigma}{dT} = \int_{E_{\bar{\nu}}^{min}}^{\infty} \frac{d\sigma_e(E_{\bar{\nu}})}{dT} \, n(E_{\bar{\nu}}) \, P(E_{\bar{\nu}}, d) \, dE_{\bar{\nu}}$$

$$+ \int_{E_{\bar{\nu}}^{min}}^{\infty} \frac{d\sigma_\alpha(E_{\bar{\nu}})}{dT} \, n(E_{\bar{\nu}}) \, [1 - P(E_{\bar{\nu}}, d)] \, dE_{\bar{\nu}} \quad . \tag{8}$$

In equation (8), $\frac{d\sigma_e}{dT}$ and $\frac{d\sigma_\alpha}{dT}$ are the differential cross sections for antineutrinos of "electron" and "α" type respectively, and $E_{\bar{\nu}}^{min}$ is the minimum energy required to produce an electron of kinetic energy T.

The observed electron spectrum depends differently upon the Weinberg angle in the event of oscillations due to the occurrence of θ_w in both $\frac{d\sigma_e}{dT}$ and $\frac{d\sigma_\alpha}{dT}$. By requiring that the theoretical electron spectra agree with experiment for accepted values of $\sin^2\theta_w$, it is possible to constrain Δ^2, θ as in Figure 5. This was obtained by requiring the cross section for production of electrons with kinetic energy between 1.5 and 3.0 MeV to be consistent (within a one σ limit) with $\sin^2\theta_w \leq 0.25$. This procedure can also be conducted for comparison with Reines' other measurement of electrons between 3.0 and 4.5 MeV.[3]

4. CONCLUSIONS

We have demonstrated that reactor experiments on antineutrino induced reactions provide constraints on the parameters describing neutrino oscillations. If these experiments are considered together, it may be possible either to determine the values of $\Delta^2$and θ, or to suggest the incompatibility of one particular experiment with the rest. This analysis is more difficult if one considers the generalized mixing among three neutrinos. For this case, however, the limits on other channels of mixing provided by accelerator and meson factory experiments may be employed to simplify the analysis.

REFERENCES

[1])S. M. Bilenky and B. Pontecorvo, Physics Reports 41, 225 (1978).

[2])F. Boehm *et al.* in a contribution to the Neutrinos-79 Conference, Bergen, Norway.

[3])F. Reines, H. S. Gurr, and H. W. Sobel, Phys. Rev. Lett. 37, 315 (1976).

[4])F. A. Nezrick and F. Reines, Phys. Rev. 142, 852 (1966).

[5])E. Pasierb, H. S. Gurr, J. Lathrop, F. Reines, and H. W. Sobel, Phys. Rev. Lett. 43, 96 (1979).

[6])A. K. Mann and H. Primakoff, Phys. Rev. D 15, 655 (1977).

[7])J. Blietschau *et al.*, Nucl. Phys. B 133, 205 (1978).

[8])S. E. Willis *et al.*, Phys. Rev. Lett. 44, 522 (1980).

[9])B. R. Davis, P. Vogel, F. M. Mann, and R. E. Schenter, Phys. Rev. C 19, 2259 (1979).

[10])F. T. Avignone III and Z. D. Greenwood (University of South Carolina preprint Feb. 1980).

[11])F. T. Avignone III and L. P. Hopkins, in Neutrinos-78, Proceedings of the International Conference on Neutrino Physics and Astrophysics Purdue, 1978, edited by E. C. Fowler (Purdue Univ. Press, Lafayette, Indiana, 1978), p. C42.

[12])F. Reines, private communication.

FIGURE CAPTIONS

Fig. 1 The effect of neutrino oscillations on the reactor anti-neutrino spectrum. Oscillations characterized by $\Delta^2 = 0.4\ eV^2$, $\sin^2 2\theta = 1.0$, d = 11.2 m. Full curve-without oscillations; dashed curve-with oscillations.

Fig. 2 Effect of oscillations on positron spectrum in inverse neutron decay. Oscillated reactor $\bar{\nu}_e$ spectrum characterized by $\Delta^2 = 0.4\ eV^2$, $\sin^2 2\theta = 1.0$, d = 11.2 m. E_e+ is positron kinetic energy; rate is in arbitrary units. Full curve-without oscillations; dashed curve-with oscillations.

Fig. 3 Values of Δ^2, θ consistent with hypothetically measured e^+ spectrum - dashed region. Obtained by χ^2 test with theoretically oscillated spectra of Davis-Vogel. "Experimental" e^+ spectrum has nearly the same shape as the full curve in Fig. 2. It lies somewhat below the curve for $E_e+ > 4$ MeV, and has average experimental errors $\sim$ 25%.

Fig. 4 Values of Δ^2, θ consistent with R between 0.6 and 0.9-dashed region. R is defined for the deuteron disintegration reactions by Eq. (7), and the spectra used are those of Davis-Vogel.

Fig. 5 Values of Δ^2, θ consistent with measured antineutrino-electron scattering cross-section, and $\sin^2 \theta_w \leq 0.25$. Dashed region- allowed values with cross section within one standard deviation of experiment for electron kinetic energy between 1.5 and 3.0 MeV.

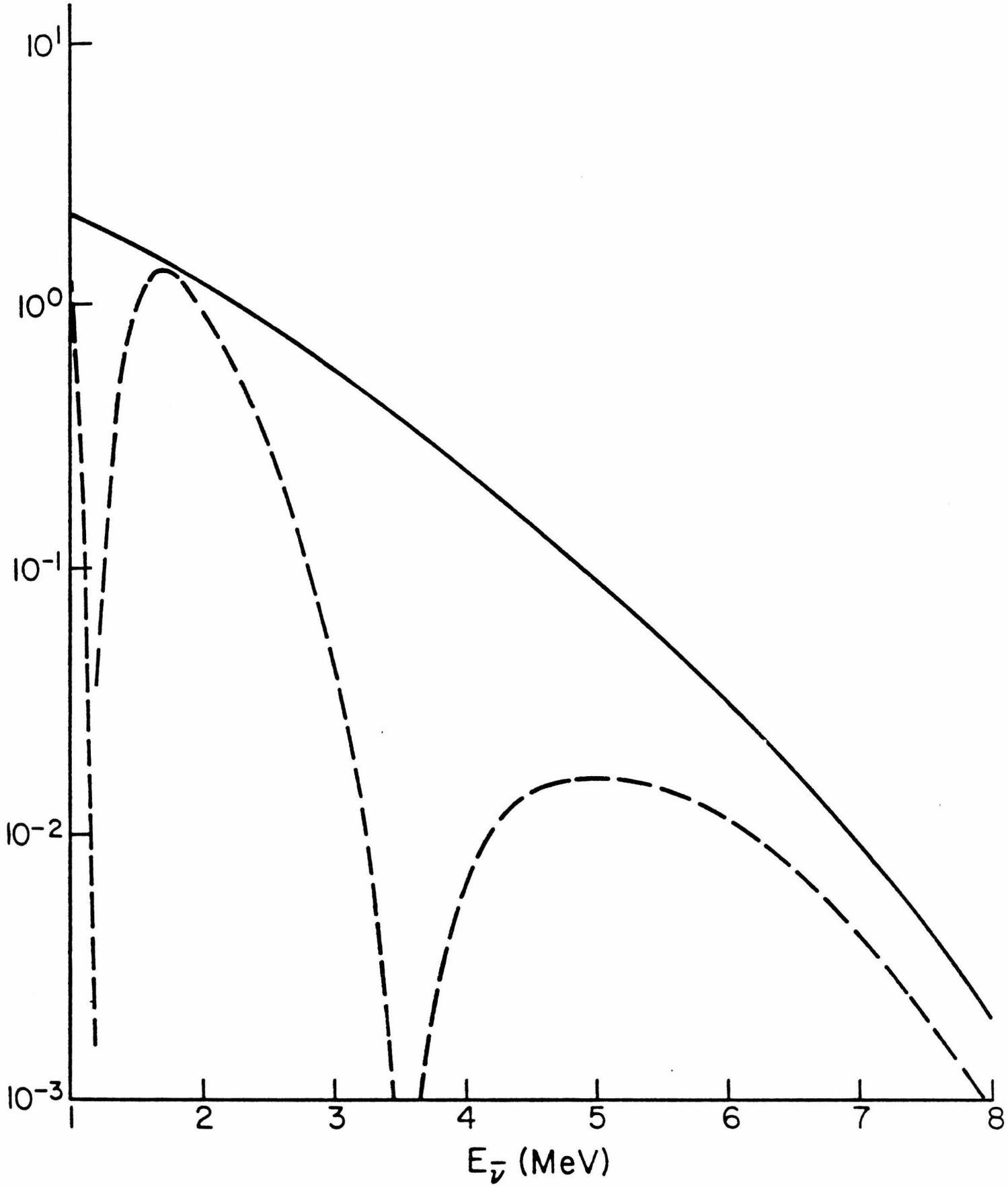

Fig. 1

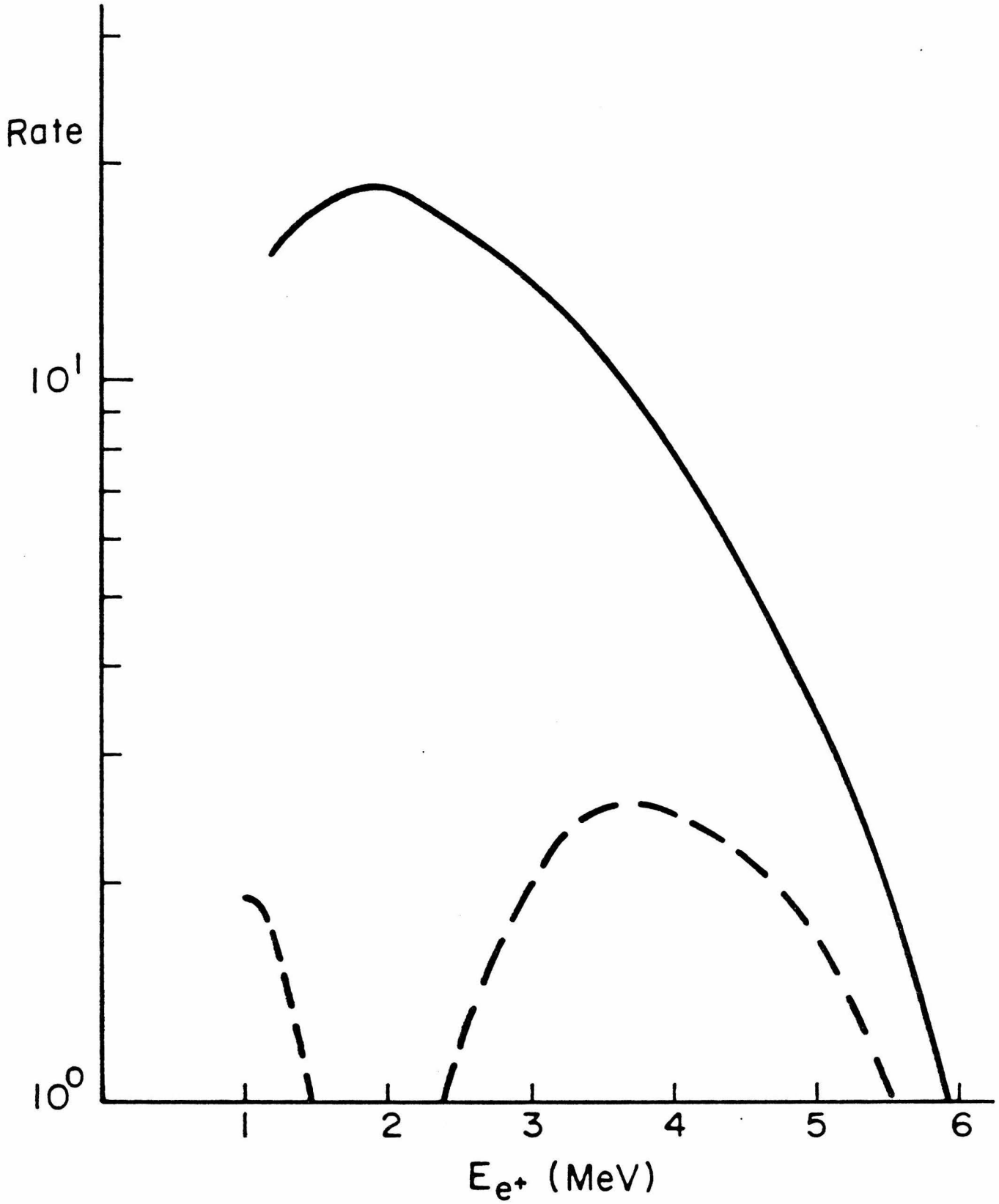

Fig. 2

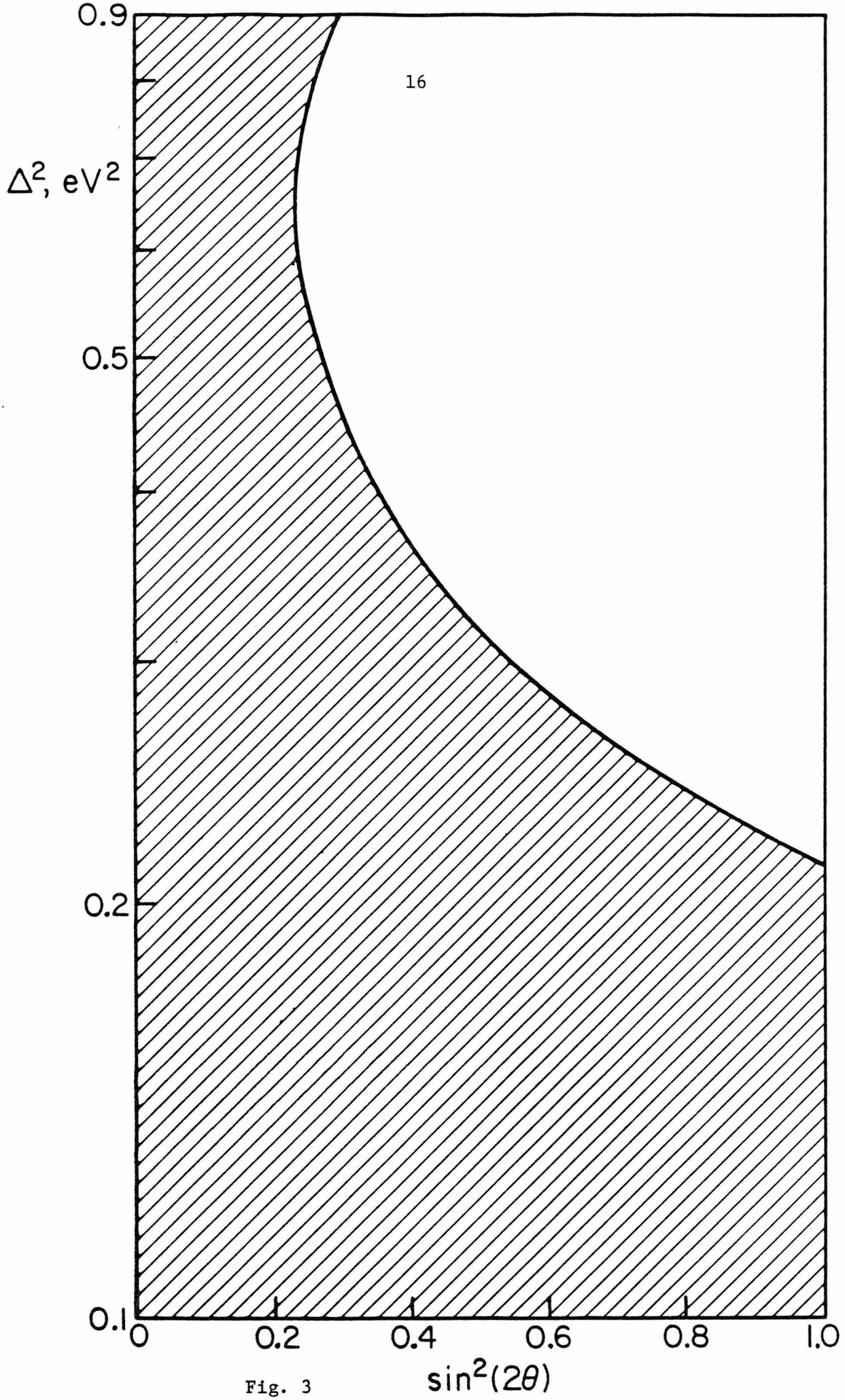

Fig. 3

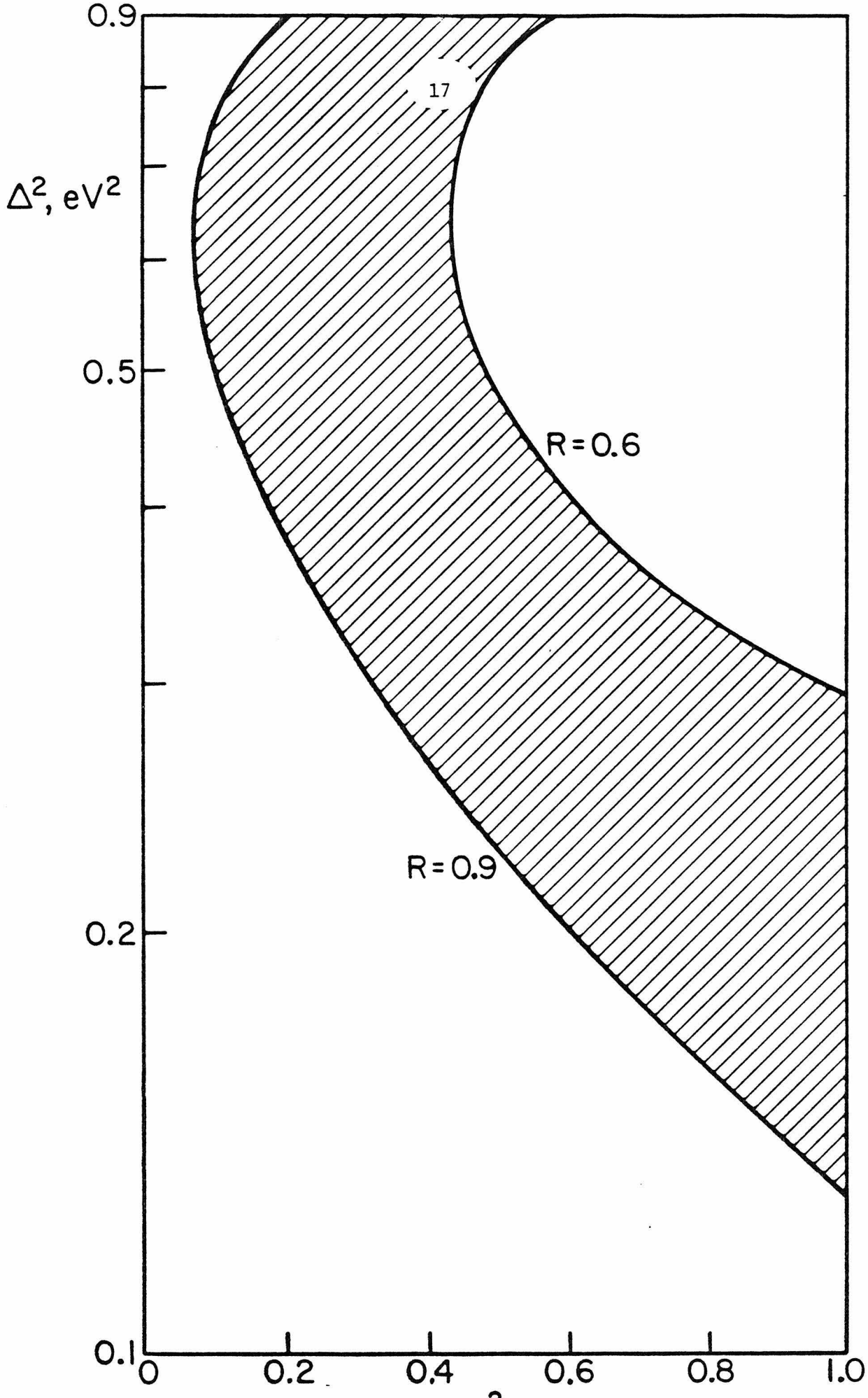

Fig. 4

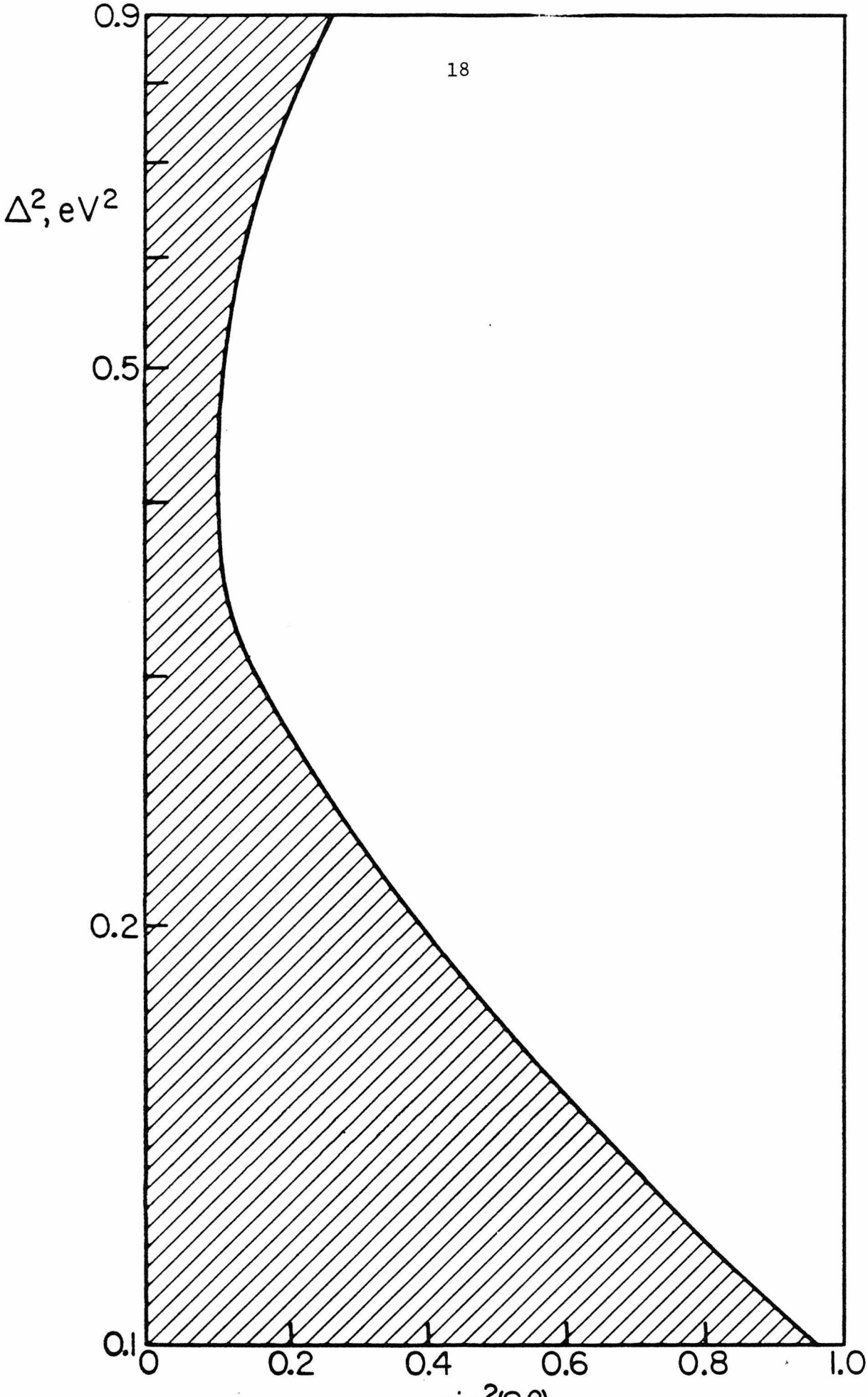

Fig. 5

CHAPTER 2

REACTOR ANTINEUTRINO SPECTRA AND THEIR APPLICATION TO ANTINEUTRINO INDUCED REACTIONS

This Chapter, with few modifications, originally appeared June 1979 in Physical Review C, Volume 19, pages 2259-2266.

Reactor Antineutrino Spectra and their Application to Antineutrino Induced Reactions

B. R. Davis, and P. Vogel
California Institute of Technology
Pasadena, California 91125

F. M. Mann and R. E. Schenter
Hanford Engineering Development Laboratory
Richland, Washington 99352

Abstract:

The knowledge of reactor antineutrino spectra is necessary for the interpretation of weak-interaction experiments located at nuclear reactors. We calculate the antineutrino and electron spectra accompanying thermal neutron fission of ^{235}U and ^{239}Pu for various irradiation times. It is stressed that the higher energy part ($E \gtrsim 4$ MeV) of the spectra depends sensitively on the beta-decay characteristics of fission products with experimentally unknown decay schemes. We also discuss the accuracy of a semiempirical conversion of the electron spectrum into the antineutrino spectrum. The resulting $\bar{\nu}_e$ spectra are used to calculate cross sections and reaction rates for the inverse neutron beta decay, weak charged and neutral current induced deuteron disintegration, and the antineutrino-electron scattering.

Keyword abstract:

[RADIOACTIVITY, FISSION ^{235}U, ^{239}Pu; antineutrino and electron spectra calculated. σ for $\bar{\nu}$ induced reactions analyzed.]

1. INTRODUCTION

Valuable information about the structure of weak neutral and charged currents can be derived from the study of neutrino induced reactions. These reactions may be also used as a source of information about the fundamental properties of the neutrino[1]), such as possible neutrino oscillations. Nuclear reactors, as sources of electron antineutrinos, give fluxes of the order $\sim 10^{13}\ \bar{\nu}/cm^2$-sec at distances $\sim$ 10 m from the reactor core. These antineutrinos have an energy spectrum peaked at very low energies ($\sim$0.3 MeV) and extending up to $\sim$10 MeV, characteristic of the β^- decay of the fission products.

Table 1 lists the antineutrino induced reactions studied at nuclear reactors. Three of the reactions listed in the table were actually observed. The first one, the inverse beta-decay of the neutron, was observed in the pioneering work of Reines and his collaborators. The most recent measurement of the total cross section[2]) has an accuracy of 15%. The charged current deuteron disintegration was observed by Jenkins *et al.*[3]) with $\sim$ 50% accuracy, and $\bar{\nu}$-electron scattering was recently observed by Reines *et al.*,[4]) with 25% accuracy. All four reactions listed in the table are currently being studied again in a new generation of experiments, and more detailed information is expected. For example, it seems feasible to determine not only the total cross section of the inverse neutron beta-decay, but also the positron spectrum with accuracy better than 10%.

In order to make useful conclusions about the underlying fundamental weak interactions, one has to know the spectrum of antineutrinos impinging on the target, with accuracy comparable to, or better than, the accuracy of

the measured cross sections. Thus a considerable effort was devoted in the past to the problem of determining the antineutrino spectra.

There are basically two methods of approach. The first one, developed in Refs. 5 and 6, uses the experimentally determined electron spectrum and converts it into the antineutrino spectrum. We shall discuss this method in greater detail in Section 3. The second method is seemingly the obvious one. A catalog of all fission fragments and their yields is made, including all the beta decay branches. Using the allowed Coulomb corrected spectral shape, one adds the contributions of all of them. Such a calculation was first performed by King and Perkins[7]. Later calculations, with more complete experimental data, were reported by Avignone and his collaborators, Refs. 8-10, and by Borovoi, Dobrynin and Kopeikin[11]. The main problem, as will be seen below, is insufficient knowledge of beta decay schemes of fission fragments with large Q values and correspondingly short lifetimes.

In this work we report the results of our calculations of antineutrino spectra and their application to the interpretation of antineutrino induced reactions. Our results differ substantially from those of Refs. 9-11. We also believe that the previously reported theoretical uncertainties[9] are too optimistic, and we attempt to estimate these uncertainties in a more realistic way. Preliminary results of our work were reported earlier[12].

While our calculations were in progress, we learned that another group, Rudstam and Aleklett[13], also calculated the reactor antineutrino spectra. Their conclusions are quite similar to ours; in particular they predict fewer high energy antineutrinos than Refs. 9-11.

In the past it was customary to normalize the calculated spectra and cross-sections per fission antineutrino. However, while the number of fissioning nuclei per second is usually accurately known, the total number of antineutrinos is much more uncertain. Moreover, as seen in Table 1, only the approximately 30% of $\bar{\nu}$'s with energies above $\sim$ 2 MeV are relevant for our purpose. Thus, in the following we report all our results "per fission" and avoid the largely misleading normalization "per antineutrino".

2. CALCULATION OF THE SPECTRA

The antineutrino spectrum is given by

$$N(E_{\bar{\nu}}) = \sum_n \lambda^n_{Z,A} C^n_{Z,A}(t) \sum_i b_{n,i}(E^i_o)\ P(E_{\bar{\nu}}, E^i_o, Z). \qquad (1)$$

Here $C^n_{Z,A}(t)$ is the concentration of nucleus Z,A after exposure time t and $\lambda^n_{Z,A}$ is the corresponding decay constant. In our calculation we have used the thermal neutron fission yields of the nuclear data file ENDF/B-V (Evaluated Nuclear Data File version V)[14]. The effect of delayed neutrons was included explicitly. The transmutations of fission fragments by reactor neutrons was also included; neutron flux of 3×10^{13} n/cm^2 sec was assumed. The fission yields of the nuclei with large Q values are almost independent of this effect.

The quantities $b_{n,i}(E^i_o)$ in Eq. (1) are branching ratios for the i-th branch with the maximal electron energy $E^i_o = Q_n + m_e c^2 - E^i_{exc}$, where Q_n is the Q-value of the species n, and E^i_{exc} is the excitation energy in the daughter nucleus. They are normalized such that $\sum_i b_{n,i}(E^i_o) = 1$, except

for isomeric states, where the sum is smaller than one due to the γ-decay.

We assume that all branches have the allowed spectral shape, i.e.,

$$P(E_{\bar{\nu}}, E_o, Z) = kE_{\bar{\nu}}^2(E_o - E_{\bar{\nu}})^2 \; G(E_o - E_{\bar{\nu}}, Z), \qquad (2)$$

where P is normalized to unity (k is the normalization constant). The function G in Eq. (2) is related to the usual Fermi Coulomb function. It depends on Z and on the total electron energy $E_\beta = E_o - E_{\bar{\nu}}$ (P_β is the electron momentum).

$$G(E_\beta, Z) \equiv (P_\beta/E_\beta) \; F(E_\beta, Z). \qquad (3)$$

In our calculation we use usually a simple analytic approximation to G which agrees to within ∿ 5% with the corresponding exact expression.

We used the beta-decay data of ENDF/B-IV[14]). This file contains 710 fission products (including isomers), of which about 200 have complete experimentally determined decay schemes. The remaining ("unknown") were treated in the following way:

a) The Q values were checked and replaced by new experimental or systematic data whenever appropriate.

b) For ∿ 60 nuclei the continuous β-feed distributions of Aleklett *et al.*[15]) were used. These additional nuclei contribute ∿ 20% of the neutrino spectrum for energies above 4 MeV.

c) For the remaining nuclei, out of which ∿ 80 have large enough yields and Q values to contribute significantly to $\bar{\nu}$ spectra above 4 MeV, various prescriptions were used, as described below.

In the past, a simple two-branch formula[8,11]) was used for the nuclei with unknown branchings. It was assumed that there are no branches to levels above the pairing energy in the daughter nucleus (except for the odd-odd daughter nuclei). Such a prescription probably overestimates the actual branching with large endpoint energies, as demonstrated by the experimental results of Ref. 15.

Thus we adopted the assumption [15]) that the average reduced transition rate is constant, independent of the excitation energy in the daughter nucleus. This leads to the following expression for the beta feeding probability:

$$b(E_o) = k' \rho (Q + m_e c^2 - E_o) \; f(E_o, Z+1) \tag{4}$$

where k' is the normalization, $\rho(E_{exc})$ is the nuclear level density and $f(E_o, Z+1)$ is given by (note that Z is the parent nucleus charge)

$$f(E_o, Z+1) = \int_{m_e c^2}^{E_o} E_\beta^2 \; (E_o - E_\beta)^2 \; G(E_\beta, Z+1) \, dE_\beta \, . \tag{5}$$

For the nuclear level density we used the formula of Ref. 15 and parameters of Ref. 16, evaluated for I = 1 as a typical spin value. The final result is only weakly dependent on this assumption (the spectrum changes by at most 1% when I = 1 is replaced by I = 3). Formula (4) is used for excitation energies above the pairing energy P and the $b(E_o)$ for these energies are normalized to

$$\sum_{E_{exc} > P} b \, (E_o) = \alpha' \, . \tag{6}$$

The values of α' were found by averaging the results of Ref. 15. We use $\alpha' = 1$ for odd-odd daughters, $\alpha' = 0.53$ for nuclei with $Q - P \geq 5$ MeV and $A < 110$, $\alpha' = 0.36$ for $Q - P \geq 5$ MeV and $A > 110$, and $\alpha' = 0.28$ for the remaining nuclei. The remaining branching $1 - \alpha'$ was equally distributed among three hypothetical states with energies 0, P/3, 2P/3.

That the average reduced transition rate is approximately constant, is an empirical fact which follows from the study[15]) of neutron rich fission products with large Q values, i.e., the nuclei similar to the "unknown" set. Two opposing influences affect the transition rate. The level density used in Eq. (4) is an overestimate, because only states obeying the quasiparticle selection rules contribute to β decay. On the other hand, one expects an increase of transition rate with excitation energy as unhindered configurations, or the giant Gamow-Teller resonance, become populated. It is our belief that the just described prescription for estimating the unknown branching ratios is more realistic than those used before in the literature.

Examples of the calculated antineutrino and electron spectra are shown in Tables 2 and 3. Columns 2-4 in both tables are based on the present prescription for treatment of the "unknown" decay schemes. They illustrate the dependence of the spectrum on the exposure time. Note that at higher energies ($E \geq 3$ MeV) the spectra are essentially independent of the exposure time. Indeed, the high energy electrons and $\bar{\nu}$'s come from the β decay of fission fragments with large Q values and correspondingly short lifetimes. Such nuclei reach equilibrium in a short time, and their fission yields in Eq. (1) are simply the corresponding cumulative yields.

Columns 5 and 6 in both tables illustrate the sensitivity of the results to the prescription used for treatment of unknown nuclei. In particular, column 6 shows the upper bound spectrum, where we assumed (unrealistically) that all unknown nuclei decay directly to the ground state. The results in column 5 were obtained using our data file together with the two-branch prescription of Ref. 8. The differences between these results and Ref. 8 are apparently caused by the differences in input data. In particular, we include as "known" the nuclei studied in Ref. 15.

The last columns in Tables 2 and 3 show the $\bar{\nu}_e$ and electron spectra, corresponding to the thermal neutron fission of ^{239}Pu. As noted earlier[10 11]) such spectra are considerably softer. Thus, for practical applications it is very important to know the relative amount of ^{235}U and ^{239}Pu fission for each particular experiment.

In column 7 of Table 2 we show the latest results of Avignone and Hopkins[10]). Their spectrum contains considerably more high energy $\bar{\nu}_e$'s than in any other similar calculation.

The electron spectra accompanying fission may be directly measured. However, only few accurate measurements were performed for "zero cooling time" relevant for our calculations. Column 7 of Table 3 shows an example of such a spectrum measured by Tsoulfanidis *et al.*[17]). Our calculated spectrum for the same 3 hour exposure time does not agree very well with the data, particularly at lower energies ($E \leq 2$ MeV). Actually, we verified that at these low energies our calculations predict $\sim$ 30% fewer electrons at all exposure times $t \leq 8$ hours, independent of the prescription used for the "unknown" nuclei. The situation is better at higher energies,

which are more relevant for the antineutrino reactions. For $2 < E \leq 6$ MeV, the calculated spectrum using our prescription (Column 2, Table 3) is only $\sim 10\%$ below the data[17]). We can only speculate about the source of the low energy discrepancy. Let us note, however, that the experimental electron spectra were actually determined in two separate experiments. The low energy data come directly from Ref. 17, while the high energy electrons were measured earlier[18]) and reanalyzed. It seems that the earlier spectra of Ref. 18 contain fewer electrons than the corresponding numbers in Tables I and II of Ref. 17. The discrepancy between the exposure time dependence of the low energy electron spectra calculated by us and measured in Refs. 17 and 18, stresses the need for new accurate measurements.

There are various sources of uncertainty in the resulting spectra. One possible source of error is the actual experimental error in branchings for "known" nuclei, and in the fission yields and Q values of all nuclei. Another source of error is associated with the experimental continuous beta-feed distributions of Aleklett *et al.*[15]). We did not attempt to include these uncertainties in our analysis, but we estimate that the corresponding error is about 10% and that it does not vary substantially with the neutrino (electron) energy. In our judgment the major uncertainty is related to the value α' (Eq.(6)) characterizing the beta-feeding above the pairing energy. Fig. 1 illustrates the corresponding spread of the resulting spectrum. The error in α' was estimated from the width of the α' distribution of nuclei studied in Ref. 15. Thus we used 40% uncertainty in α' for $Q-P > 5$ MeV and 80% in α' for $Q-P < 5$ MeV. Fig. 1 also shows how far the spectrum of Avignone and Hopkins[10]) is from our present calculation.

Fig. 2 illustrates the crucial role played by the "unknown" nuclei.

These nuclei contribute relatively little to the integral quantities, such as the total number of electrons (or $\bar{\nu}_e$), the total electron energy, and the total fission yield. Their contribution to the high energy tail of the spectrum is, however, greatly enhanced. This crucial role of the "unknown" nuclei was not sufficiently stressed in previous studies of the problem [8-11].

The actual form of the theoretical beta-feed function $b(E_o)$ (Eq. (4)) is illustrated in Fig. 3 and compared with experiment[15]. The agreement in this particular case is excellent. The qualitative features of $b(E_o)$ are similar in all nuclei. They are related to the fast increase of the nuclear level density $\rho(E_{exc})$, which competes with the fast decreasing $\sim (Q + m_e c^2 - E_{exc})^5$ spectral shape factor. Our results are relatively insensitive to the distribution of the $1 - \alpha'$ feeding among the states below the pairing energy P.

3. RELATION BETWEEN REACTOR ELECTRON AND ANTINEUTRINO SPECTRA

In the β^- decay of a fission product with a given Q value two particles are emitted: An electron of total energy $E_\beta = Q + m_e c^2 - E_{\bar{\nu}}$ and an antineutrino with energy $E_{\bar{\nu}}$. Obviously, both spectra are determined by the same function $n(Z, E = Q + m_e c^2)$ which describes the distribution of end points in Z and E. The question arises whether, given an experimentally measured electron spectrum, one can infer the function n(Z,E) and determine the antineutrino spectrum. It was our objective to study quantitatively the accuracy of this method, first proposed by Muelhause and Oleksa[5], and further developed by Carter *et al.*[6].

Following Ref. 6 we shall neglect the Z dependence of n(Z,E) and assume that the number of electrons per MeV is equal to

$$Y(E_\beta) = \int_{E_\beta}^{\infty} dE\, n(Z, E)\; k(Z,E) \cdot E_\beta^2 (E - E_\beta)^2\, G(E_\beta, Z), \tag{7}$$

where k(Z,E) is the normalization for the allowed spectrum.
The endpoint distribution n(Z,E) is then equal to

$$n(Z,E) = -\frac{1}{2k(Z,E)} \frac{d^3}{dE^3} \left\{ \frac{Y(E)}{E^2 G(E,Z)} \right\}. \tag{8}$$

An example of the resulting endpoint distribution n(Z,E) is shown in Fig. 4 for two extreme values of Z. We see that this function is practically independent of Z, thus giving a posteriori justification of Eq. (7). We have verified that the function n(Z,E) depends only slightly on Z in all the cases we studied.

Thus it appears that we have arrived at a "universal" endpoint distribution function, which can now be applied to generate the reactor antineutrino spectrum

$$X(Z, E_{\bar\nu}) = \int_{E_{\bar\nu} + m_e c^2}^{\infty} dE\, n(Z,E) \cdot k(Z,E)\; E_{\bar\nu}^2 (E - E_{\bar\nu})^2\, G(E - E_{\bar\nu}, Z). \tag{9}$$

Since the ^{235}U fission products are distributed in two peaks at low and high mass regions, it seems reasonable to express the reactor $\bar\nu_e$ spectrum as the average of the two spectra evaluated at the mean charge of each peak. The final antineutrino spectrum depends only slightly on the actual

prescription for this averaging, as long as both peaks in the fission fragment distribution are included with equal weight.

We tested quantitatively the accuracy of the above procedure for various electron spectral shapes $Y(E_\beta)$. This was done by generating both the electron and antineutrino spectra using the program described in Sect. 2, and then converting the electron spectrum into the antineutrino spectrum. We find that the conversion program has accuracy of better than 10% at each energy up to ~ 7.5 MeV for typical electron spectra. This is illustrated in Fig. 5, where the relative error of conversion is plotted:

$$\Delta = \frac{N_{conv.}(E_{\bar{\nu}}) - N_{gener.}(E_{\bar{\nu}})}{N_{gener.}(E_{\bar{\nu}})} \qquad (10)$$

Such a conversion method, together with an accurate experimental e^- spectrum, may be a valuable tool in the attempt to derive a correct $\bar{\nu}_e$ spectrum.

4. APPLICATION TO ANTINEUTRINO INDUCED REACTIONS

In this section we apply the resultant antineutrino spectrum to the calculation of the corresponding reaction rates. We discuss in more detail the four antineutrino induced reactions listed in Table 1. To stress the sensitivity of the results to the shape and magnitude of the reactor antineutrino spectrum, we compare our present results with the most recent calculations of Ref. 10. We do not show the "theoretical error" in our plots. One should remember, however, that we estimate

ı theoretical uncertainty gradually increasing from $\sim$ 10% at

$E_{\bar{\nu}}$ = 2 MeV to $\sim$ 30% at $E_{\bar{\nu}}$ = 8 MeV.

The inverse neutron beta decay, $\bar{\nu}_e + p \rightarrow n + e^+$, is the reaction rith the largest cross section on our list. For monoenergetic anti-ıeutrinos, the cross section is given by the expression

$$\sigma(E_{\bar{\nu}}) = 8.85 \times 10^{-44} \; (E_{\bar{\nu}} - (M_n - M_p)c^2) \left[(E_{\bar{\nu}} - (M_n - M_p)\, c^2)^2 - (m_e c^2)^2 \right]^{\frac{1}{2}} \text{cm}^2, \qquad (11)$$

/here energies are measured in MeV and

$$8.85 \times 10^{-44} \text{ cm/MeV}^2 = \frac{G^2}{\pi} (\hbar c)^2 \; (f^2 + 3g^2), \; g/f = 1.23, \; G = \frac{1.0 \times 10^{-5}}{(M_p c^2)^2}. \qquad (12)$$

Fig. 6 shows the cross section for a given positron kinetic energy E_{e^+} (the small neutron recoil is neglected), that is (11) multiplied by the corresponding $\bar{\nu}_e$ spectrum. When integrated over all positron energies one obtains the total cross section in units of 10^{-44} cm^2/fission equal to 60 for the $\bar{\nu}_e$ spectrum calculated here and 80 for the $\bar{\nu}_e$ spectrum of Ref. 10. The experiment[2]) gives 56 ± 8. This reaction is also of interest as a proposed detector of possible neutrino oscillations[19,20]).

The antineutrino electron scattering, $\bar{\nu}_e + e^- \rightarrow \bar{\nu}_e + e^-$, is perhaps the most interesting on our list. By measuring the differential cross section, i.e., the electron recoil spectrum, one can obtain valuable information about the structure of the weak interaction Hamiltonian. For monoenergetic $\bar{\nu}_e$'s and electron recoil kinetic energy T, the cross section is given by the expression[4])

$$\frac{d\sigma(E_{\bar{\nu}})}{dT} = \frac{G^2 m_e c^2}{2\pi} (\hbar c)^2 \left\{ (C_V + C_A)^2 + (C_V - C_A)^2 \left(1 - \frac{T}{E_{\bar{\nu}}}\right)^2 + \frac{m_e c^2 T}{E_{\bar{\nu}}^2} (C_A^2 - C_V^2) \right\} . \quad (13)$$

Here $C_V (C_A)$ is the vector (axial vector) coupling constant. In the Weinberg-Salam theory one has $C_A = -1/2$, $C_V = 1/2 + 2 \sin^2 \theta_W$. The observable electron spectrum is proportional to the cross section

$$\frac{d\sigma}{dT} = \int_{E_{\bar{\nu}}^{min}}^{\infty} \frac{d\sigma(E_{\bar{\nu}})}{dT} N(E_{\bar{\nu}}) \, dE_{\bar{\nu}} , \quad (14)$$

where $E_{\bar{\nu}}^{min}$ is the minimum antineutrino energy allowed by kinematics. In practice, the antineutrinos in the vicinity of minimal energy give the largest contribution to the integral (14). Fig. 7 shows the cross section (14) integrated over an interval 1.5 MeV wide in the electron kinetic energy. Future accurate measurements of the recoil electrons in these energy intervals, combined with an accepted antineutrino spectrum, may constitute an effective test of the Weinberg-Salam theory in the leptonic sector.

The two deuteron-disintegration reactions have higher thresholds (2.23 MeV for the neutral current induced reaction, 4.03 MeV for the charged current reaction) than the inverse neutron beta decay. This is one of the reasons for the corresponding cross sections being smaller. Another reason is the small overlap between the initial bound and final continuum state. Only the axial vector part of the weak current contributes to the deuteron disintegration at reactor antineutrino energies. In our calculation we use the cross section formulas of Ahrens and Lang[21]). The

formulas were derived assuming zero effective range of the nuclear forces. The meson exchange effects, known to contribute $\sim$ 10% to the related n-p radiative capture, are also neglected. All of these approximations do not affect the main features of our results.

For the charged current reaction, $\bar{\nu} + d \rightarrow n + n + e^+$, we show in Fig. 8 the predicted positron spectrum:

$$\frac{d\sigma}{dE_{e^+}} = \int_{E_{e^+} + E_T}^{\infty} \frac{d\sigma(E_{\bar{\nu}})}{dE_{e^+}} N(E_{\bar{\nu}})\, dE_{\bar{\nu}} , \tag{15}$$

where E_T is the reaction threshold.

The total cross section in 10^{-44} cm^2/fission is equal to 1.2 for the present $\bar{\nu}_e$ spectrum and 2.1 for that of Ref. 10. The large difference between these two cross sections is related to the threshold; the $\bar{\nu}_e$ spectra differ more at higher energies. The experimental cross section[3]) is 1.8 ± 0.9.

For the neutral current deuteron disintegration, $\bar{\nu} + d \rightarrow p + n + \bar{\nu}$, we show in Fig. 9 the reaction rate

$$R = \sigma(E_{\bar{\nu}}) \cdot N(E_{\bar{\nu}}). \tag{16}$$

The total cross section in 10^{-44} cm^2 is equal to 2.9 for the present $\bar{\nu}_e$ spectrum and 4.3 for the $\bar{\nu}_e$ spectrum in Ref. 10. There are no experimental data on this reaction at the present time.

5. SUMMARY

We have verified that the high energy tail of the antineutrino and electron spectra depends sensitively on the treatment of nuclei with unknown beta decay schemes. The simple two branch formula for such decays, used in previous calculations, considerably underestimates beta branching to states above the pairing energy and, consequently, overestimates the number of high energy antineutrinos and electrons.

Besides using the most up-to-date experimental data available on known beta decay schemes, fission yields, nuclear masses, and Q-values, we also include in our calculation the continuous beta-feed results of Ref. 15. Thus our calculation reduces, to the greatest extent possible, the uncertainties present in the resulting spectra. Our treatment of the "unknown" nuclei is based on experimental studies of neutron-rich, high Q-value nuclei, and would thus appear to be quite realistic.

We stress the potential importance of experimentally determined reactor electron spectra. An accurate spectrum can be compared with our results, testing our input data and prescription for unknown nuclei. It can also be used, in conjunction with the semiempirical conversion procedure discussed in Sect. 3, to obtain the antineutrino spectra directly.

The application of our calculation to antineutrino induced reactions shows how sensitively the final measured cross sections depend on the input spectrum. Among the reactions we discussed, the situation is most critical in the case of the charged current deuteron disintegration, where the total cross section differs by a factor of two between our results and those of Ref. 10. On the other hand, the difference is considerably

less ($\sim$30%) in the inverse neutron beta decay and in the antineutrino electron scattering.

Acknowledgments:

We would like to thank Dr. Charles Reich for his help in preparing the input data and for numerous valuable discussions. We also benefited from discussions with Professors F. Boehm, W. A. Fowler and V. Telegdi. One of the authors, P. V., would like to acknowledge the hospitality of the Aspen Center of Physics. This work was supported by DOE (EY-76-C-03-0063 and EY-76-C-14-2170) and NSF (PHY 76-83685).

REFERENCES

[1] S. M. Bilenky and B. Pontecorvo, Phys. Lett. 41C, 225 (1978), and references therein.

[2] F. A. Nezrick and F. Reines, Phys. Rev. 142, 852 (1966).

[3] T. L. Jenkins, F. E. Kinard, and F. Reines, Phys. Rev. 185, 1599 (1969).

[4] F. Reines, H. S. Gurr, and H. W. Sobel, Phys. Rev. Lett. 37, 315 (1976).

[5] C. O. Muelhause and S. Oleksa, Phys. Rev. 105, 1332 (1957).

[6] R. E. Carter, F. Reines, J. J. Wagner, and M. E. Wyman, Phys. Rev. 113, 280 (1959).

[7] R. W. King and J. F. Perkins, Phys. Rev. 112, 963 (1958).

[8] F. T. Avignone III, Phys. Rev. D2, 2609 (1970).

[9] F. T Avignone III and Z. D. Greenwood, Phys. Rev. D17, 154 (1978).

[0] F. T Avignone III and L. P. Hopkins, in Neutrinos-78, E. C. Fowler, editor, Purdue University 1978, p. C42.

[1] A.A. Borovoĭ, Yu. L. Dobrynin, and V. I. Kopeĭkin, Sov. J. Nucl. Phys. 25, 144 (1977).

[2] B. R. Davis, P. Vogel, F. M. Mann, and R. E. Schenter, BAPS 23, 927 (1978).

[3] G. Rudstam and K. Aleklett, preprint Studsvik Sci. Res. Lab., 1978.

[4] Fission Product Decay Library of the Evaluated Nuclear Data File, Versions IV and V. Available from, and maintained by, the National Nuclear Data Center (NNDC) at the Brookhaven National Laboratory.

[5] K. Aleklett, G. Nyman, and G. Rudstam, Nucl. Phys. A246, 425 (1975).

[6] J. W. Truran, A. G. W. Cameron, and E. Hilf, CERN 70-30, Vol. 1, p. 275 (1970).

[17])N. Tsoulfanidis, B. W. Wehring, and M. E. Wyman, Nucl. Sci. and Eng. 43, 42 (1971).

[18])J. W. Kutcher and M. E. Wyman, Nucl. Sci. and Eng. 25, 435 (1966).

[19])F. Boehm, private communication and ILL Annual Report, Grenoble, 1977.

[20])F. Reines, in Unification of Elementary Forces and Gauge Theories, D. B. Cline and F. E. Mills, editors, Harwood Academic Publishers, London, 1978, p. 103.

[21])T. Ahrens and T. P. Lang, Phys. Rev. C3, 979 (1971).

TABLE 1. Reactor Antineutrino Induced Reactions

Reaction	σ_{tot} in 10^{-44} cm^2/fission[a)]	Threshold in MeV
$\bar{\nu} + p \rightarrow n + e^+$	60	1.8
$\bar{\nu} + d \rightarrow n + n + e^+$	1.2	4.0
$\bar{\nu} + d \rightarrow n + p + \bar{\nu}$	2.9	2.3
$\bar{\nu} + e^- \rightarrow \bar{\nu} + e^-$	0.4[b)]	1.7[c)]

a) Based on our present calculation of the antineutrino spectrum for 30 days exposure time.

b) For the Weinberg-Salam theory with $\sin^2 \Theta_W = 0.25$.

c) This is a "practical" threshold assuming that electrons with kinetic energy below 1.5 MeV are impossible to observe.

TABLE 2. Antineutrino Spectra

Energy MeV	^{235}U Exposure Time 3 hours[a]	30 days[a]	3 years[a]	Avignone Prescription[b]	Ground State Prescription[c]	Avignone Purdue[d]	^{239}Pu 7 days exposure[a]
1.0	1.56	2.23	2.38	2.12	2.10		2.7
1.5	1.35	1.56	1.65	1.55	1.53	1.64	1.34
2.0	1.05	1.16	1.21	1.18	1.18	1.33	9.82(-1)
2.5	7.66(-1	8.19(-1	8.42(-1	8.51(-1	8.61(-1		6.81(-1
3.0	5.72(-1	5.93(-1	5.95(-1	6.33(-1	6.44(-1	7.41(-1	4.88(-1
4.0	2.69(-1	2.73(-1	2.73(-1	2.96(-1	3.19(-1	3.58(-1	2.03(-1
5.0	1.02(-1	1.03(-1	1.03(-1	1.12(-1	1.37(-1	1.37(-1	6.77(-2
6.0	3.50(-2	3.50(-2	3.50(-2	4.14(-2	5.25(-2	5.73(-2	2.08(-2
7.0	1.01(-2	1.01(-2	1.01(-2	1.27(-2	1.74(-2	1.94(-2	5.03(-3
8.0	1.87(-3	1.87(-3	1.87(-3	2.78(-3	4.91(-3	5.85(-3	8.14(-4

a) Present prescription for unknown decays (see text).

b) 30 days exposure time, unknown decays treated with the two branch prescription of Ref. 8.

c) 30 days exposure time, nuclei with unknown decays allowed to decay only to the daughter ground state.

d) Calculated spectrum of Ref. 10.

TABLE 3. Electron Spectra

Total Energy MeV	^{235}U Exposure Time 3 hours[a]	30 days[a]	3 years[a]	Avignone Prescription[b]	Ground State Prescription[c]	University of Illinois Exp.[d]	^{239}Pu 7 days exposure[a]
1.0	1.93	2.87	2.99	2.75	2.72	2.72	2.65
1.5	1.49	1.81	1.92	1.78	1.76	2.09	1.57
2.0	1.10	1.23	1.28	1.24	1.24	1.37	1.04
2.5	7.85(-1	8.43(-1	8.67(-1	8.78(-1	8.84(-1	9.10(-1	7.03(-1
3.0	5.62(-1	5.87(-1	5.95(-1	6.24(-1	6.36(-1	6.08(-1	4.79(-1
4.0	2.52(-1	2.56(-1	2.56(-1	2.78(-1	3.00(-1	2.73(-1	1.89(-1
5.0	9.36(-2	9.46(-2	9.46(-2	1.04(-1	1.26(-1	1.06(-1	6.17(-2
6.0	3.18(-2	3.18(-2	3.18(-2	3.75(-2	4.74(-2	3.95(-2	1.89(-2
7.0	9.04(-3	9.04(-3	9.04(-3	1.14(-2	1.54(-2	1.35(-2	4.56(-3
8.0	1.71(-3	1.71(-3	1.71(-3	2.50(-3	4.40(-3	4.00(-3	7.57(-4

[a] Present prescription for unknown decays (see text).

[b] 30 days exposure time, unknown decays treated with the two branch prescription of Ref. 8.

[c] 30 days exposure time, nuclei with unknown decays allowed to decay only to the daughter ground state.

[d] Experimental spectrum of Ref. 17, 3 hours exposure time.

FIGURE CAPTIONS

Fig. 1. Upper and lower limits of the present calculated antineutrino spectrum (dashed curves) -see text for explanation. The full curve shows, for comparison, the spectrum calculated in Ref. 10.

Fig. 2 The relative role of "unknown" nuclei at various antineutrino energies. "f" is the fraction of the antineutrinos emitted from nuclei with unknown decay schemes. The full curve corresponds to the ground state decay of "unknown" nuclei; dashed curve was calculated with the two-branch formula of Ref. 8; dot-and dashed curve calculated with the present prescription, Eq. (4).

Fig. 3 Beta-feeding for the decay of ^{86}Br, Q = 8.0 MeV. The full histogram shows experimental data of Ref. 15 and the dotted histogram shows the calculated results using Eq. (4).

Fig. 4 The endpoint energy distribution function n(Z,E), Eq. (8) in arbitrary units. The full curve is calculated for Z = 60, the dashed curve for Z = 32. As input the electron spectrum of ^{235}U in Column 4, Table 3 is used.

Fig. 5 The deviation Δ in percent, Eq. (10), for the ^{235}U fission (3 years exposure time) -full curve, and ^{239}Pu fission (7 day exposure time) -dashed curve.

Fig. 6 Cross section for the reaction $\bar{\nu} + p \rightarrow n + e^+$ folded, with the antineutrino spectrum, in 10^{-44} cm^2/MeV·fission. The present spectrum was used to calculate the full curve, the spectrum of Ref. 10 was used in calculation of the dashed curve.

Fig. 7 The cross section for the reaction $\bar{\nu} + e^- \rightarrow \bar{\nu} + e^-$ as a function of the Weinberg angle θ_W. The lower set of curves corresponds to the integral over final electron kinetic energies T = 3 - 4.5 MeV. The upper curves are for T = 1.5 - 3 MeV. In each case the full line was calculated with the present $\bar{\nu}_e$ spectrum and the dashed line with the $\bar{\nu}_e$ spectrum of Ref. 10. The horizontal lines give the experimental limits of Ref. 4 recalculated "per fission".

Fig. 8 The cross section of the reaction $\bar{\nu} + d \rightarrow n + n + e^+$ in 10^{-45} cm^2/MeV·fission. See notation of Fig. 6.

Fig. 9 The reaction rate $\sigma(E_{\bar{\nu}}) \cdot N(E_{\bar{\nu}})$ for the reaction $\bar{\nu} + d \rightarrow n + p + \bar{\nu}$ in 10^{-45} cm^2/MeV·fission. See notation of Fig. 6.

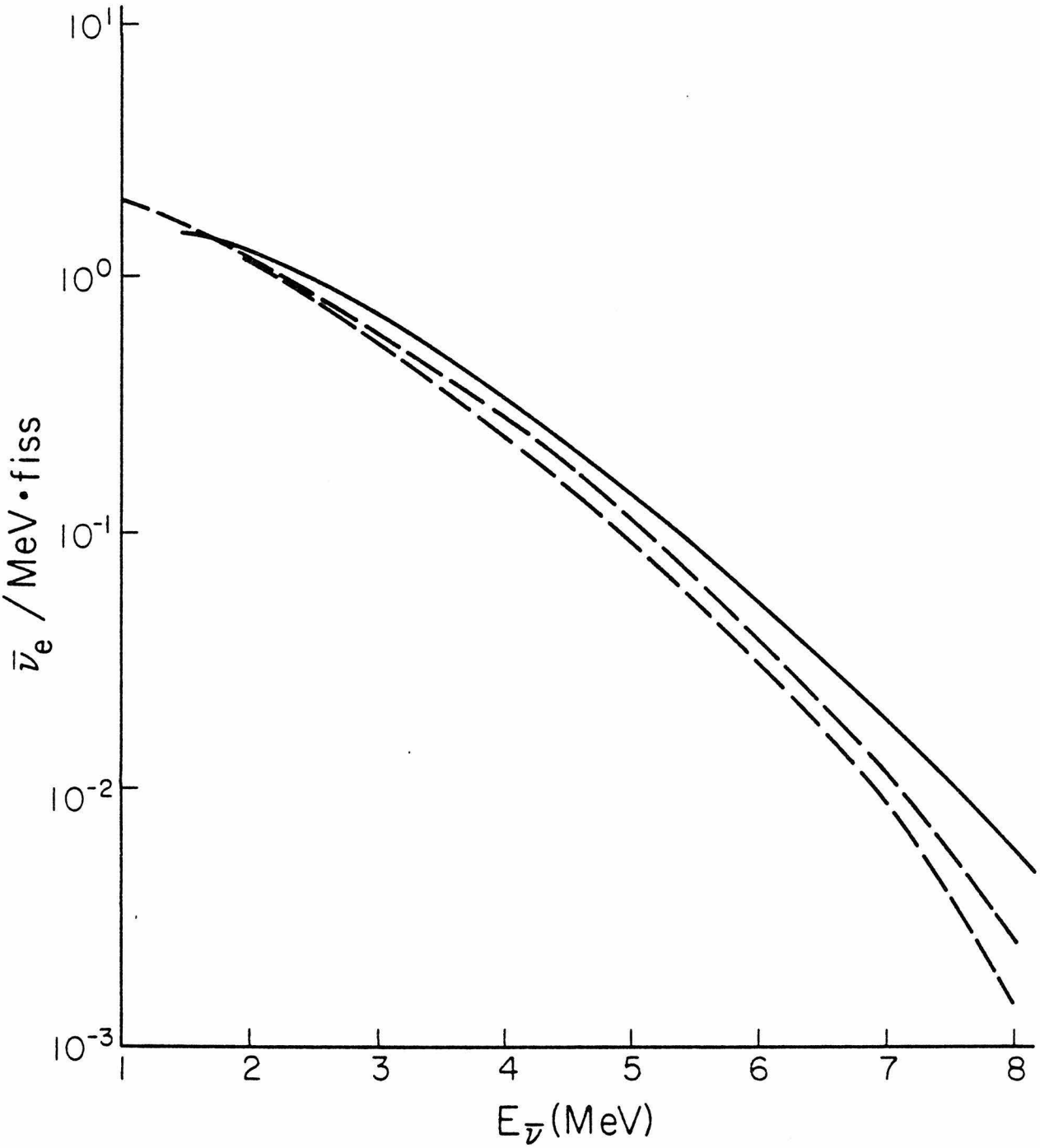

Fig. 1

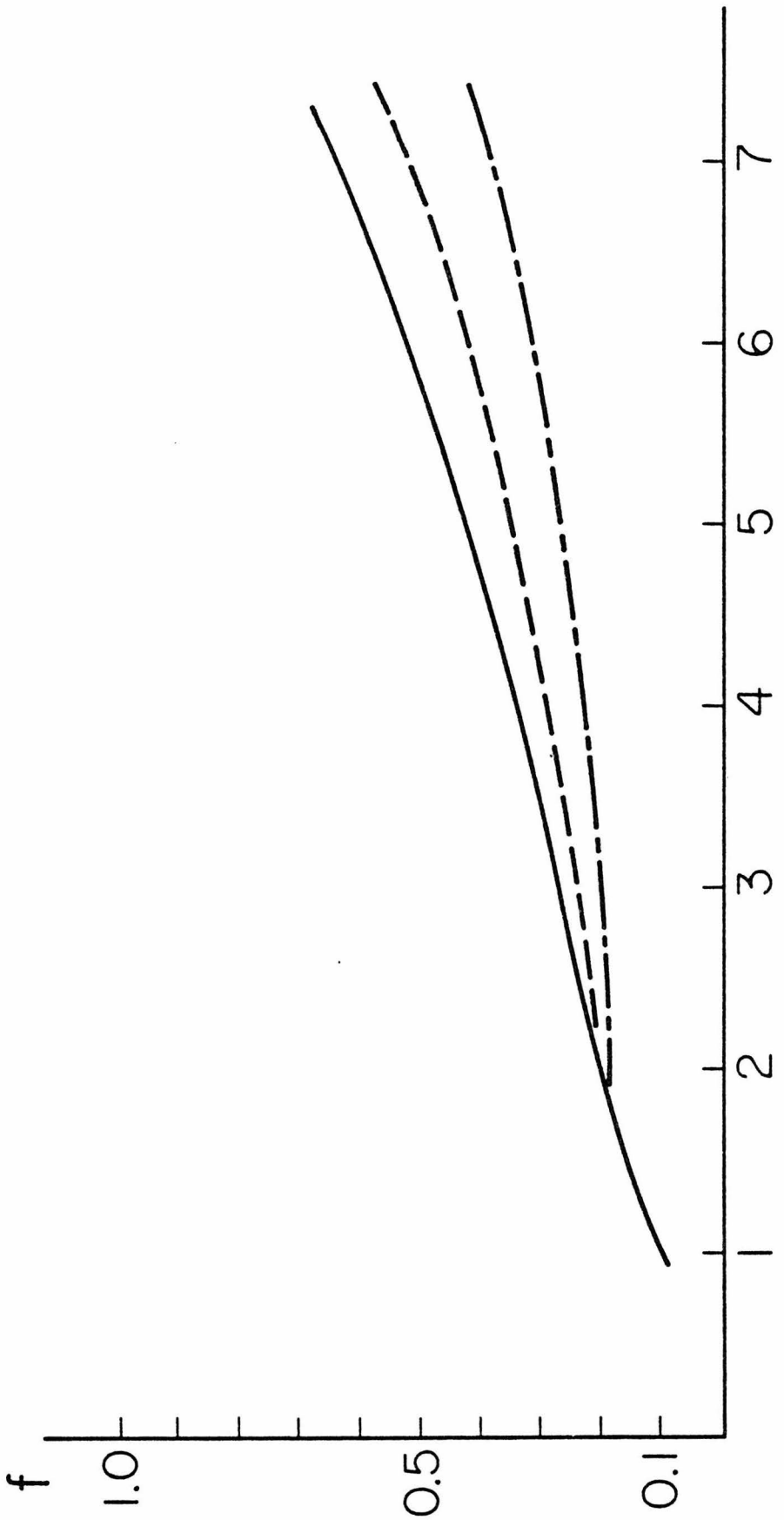

Fig. 2

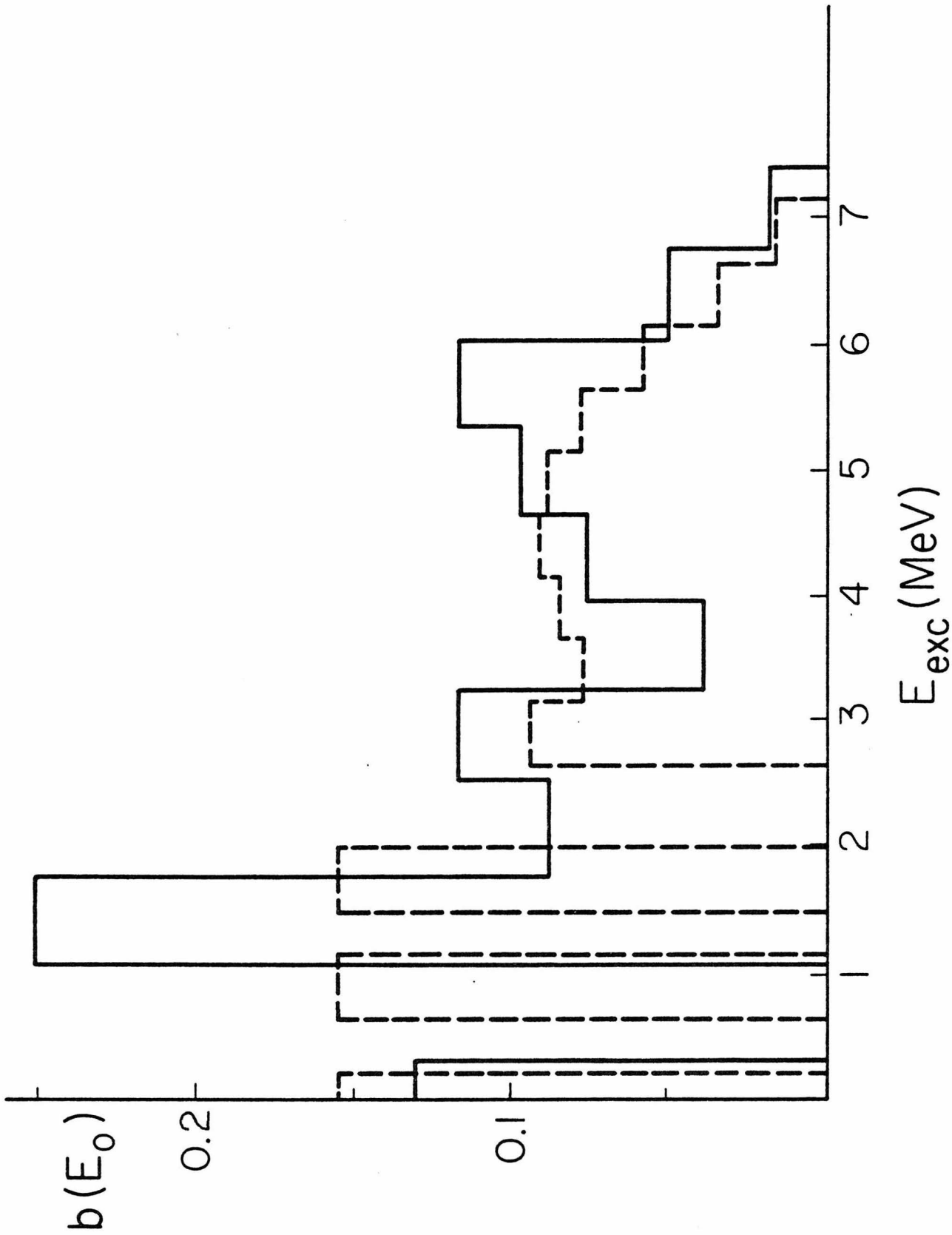

Fig. 3

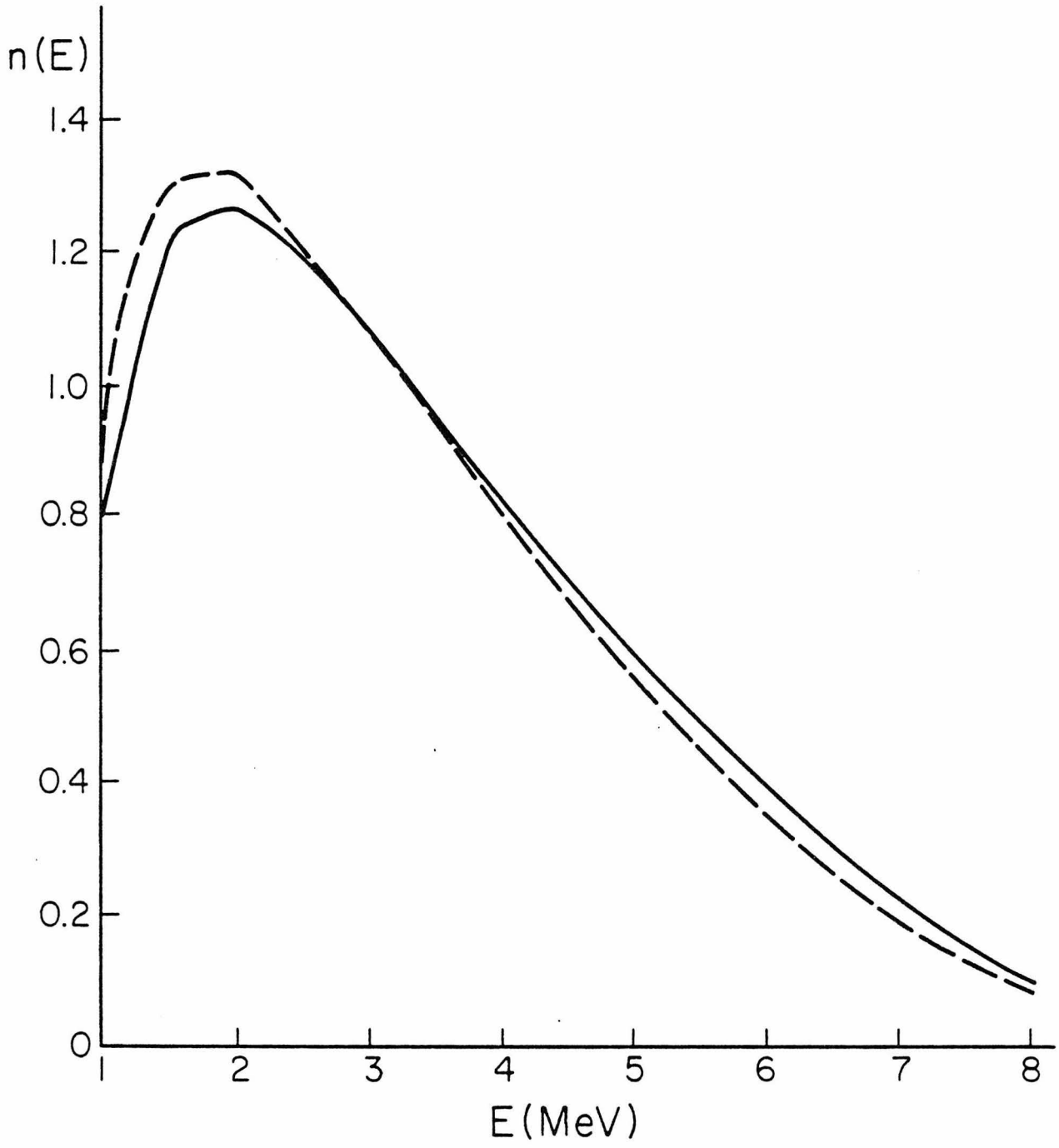

Fig. 4

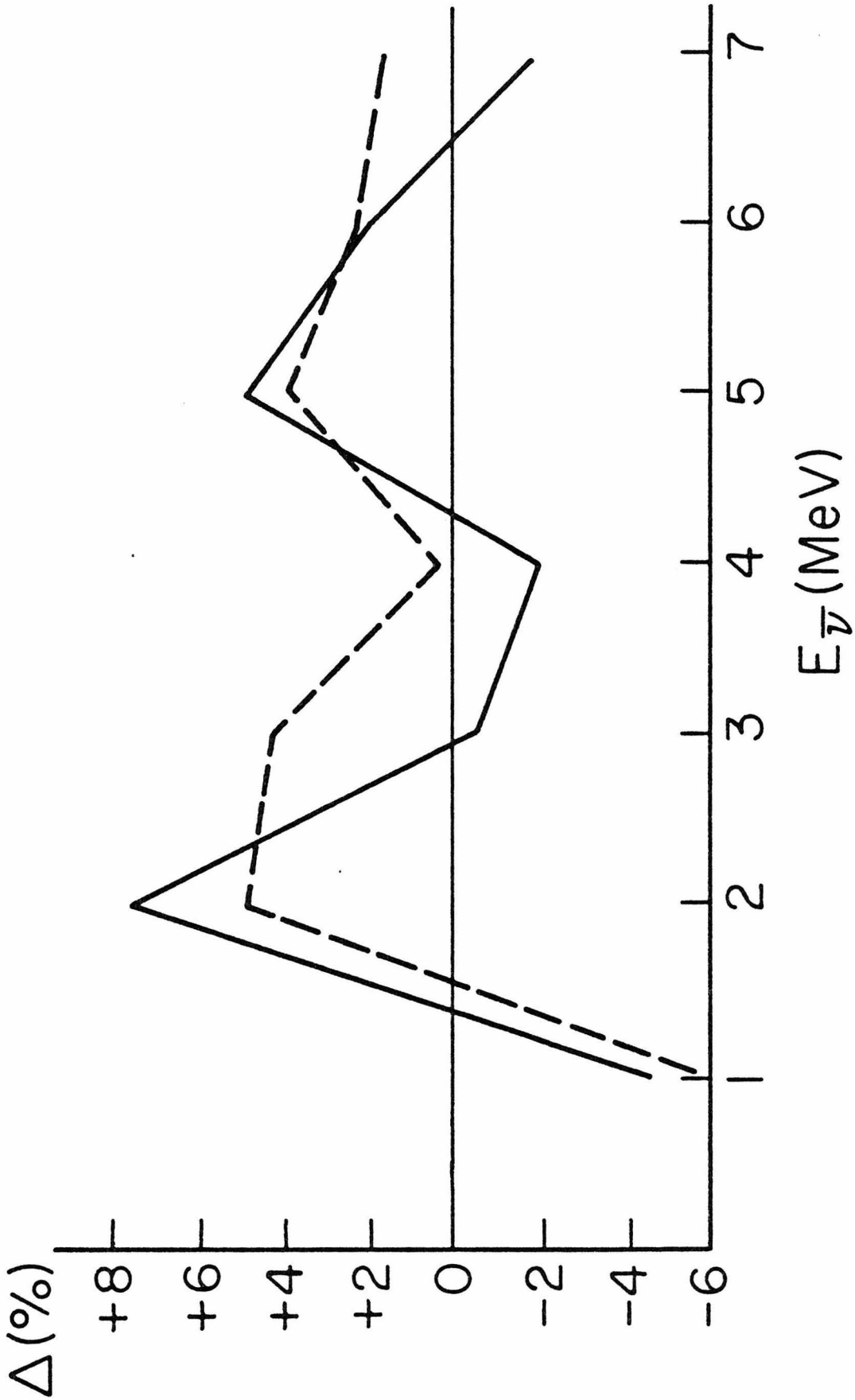

Fig. 5

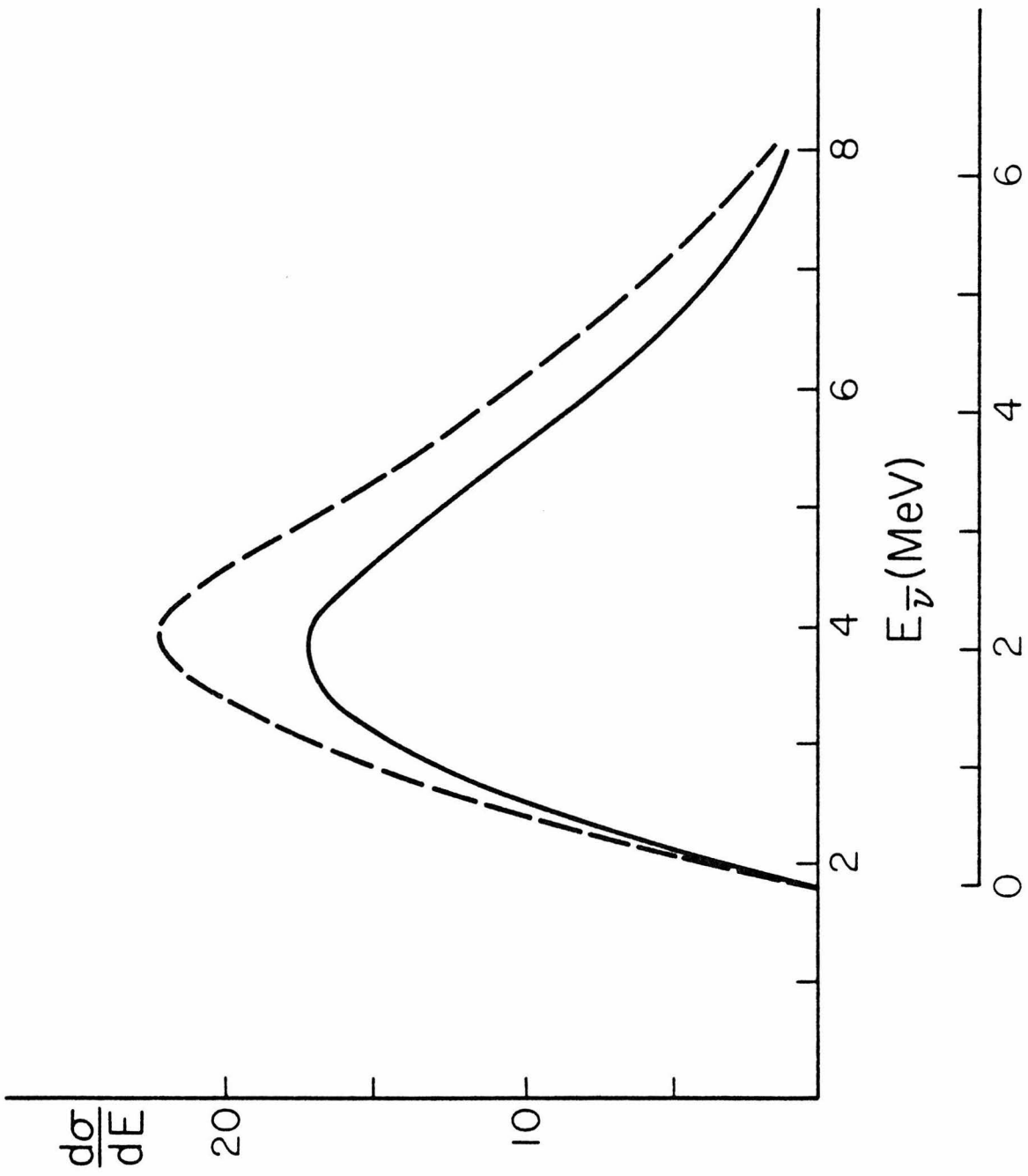

Fig. 6

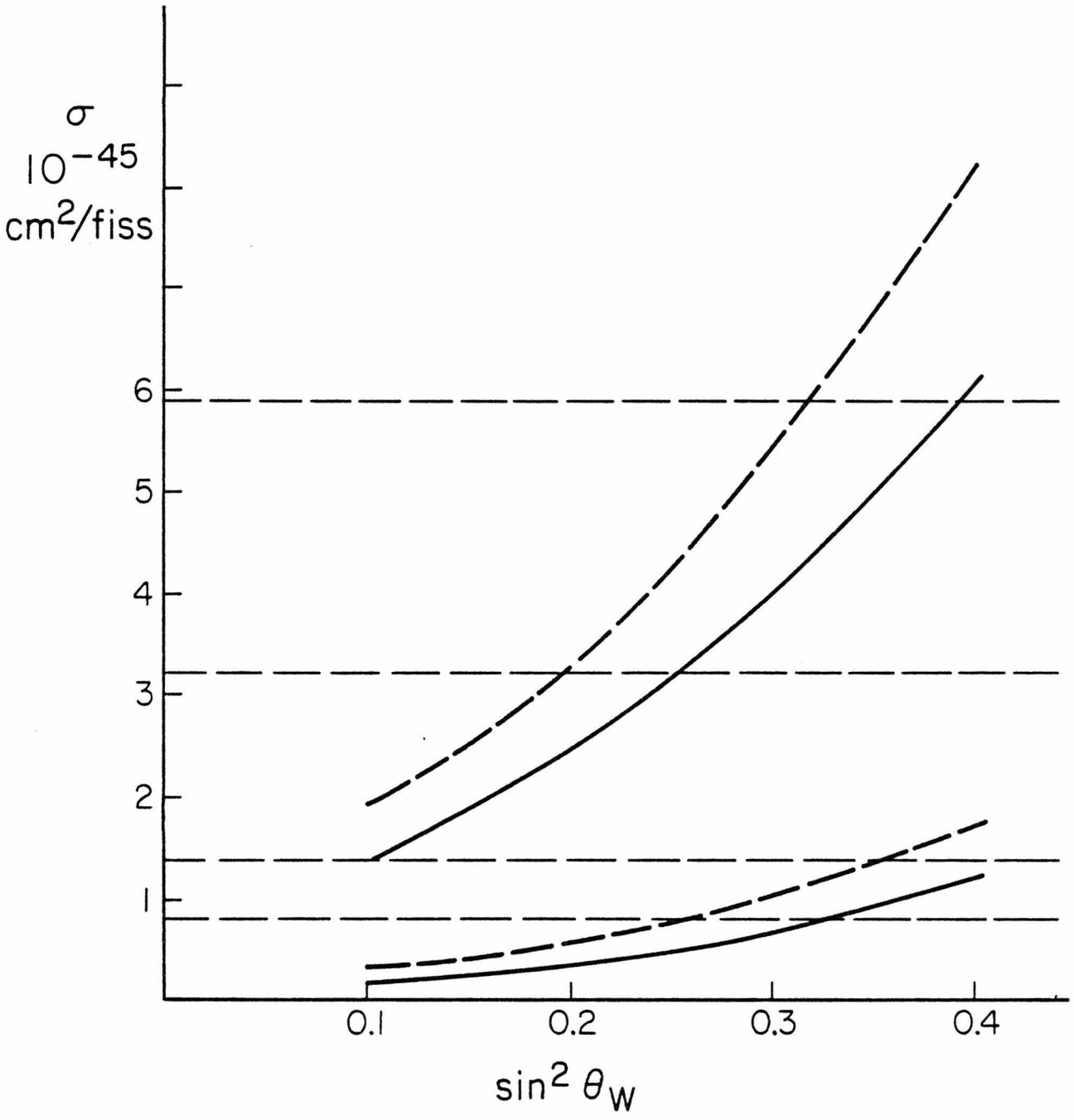

Fig. 7

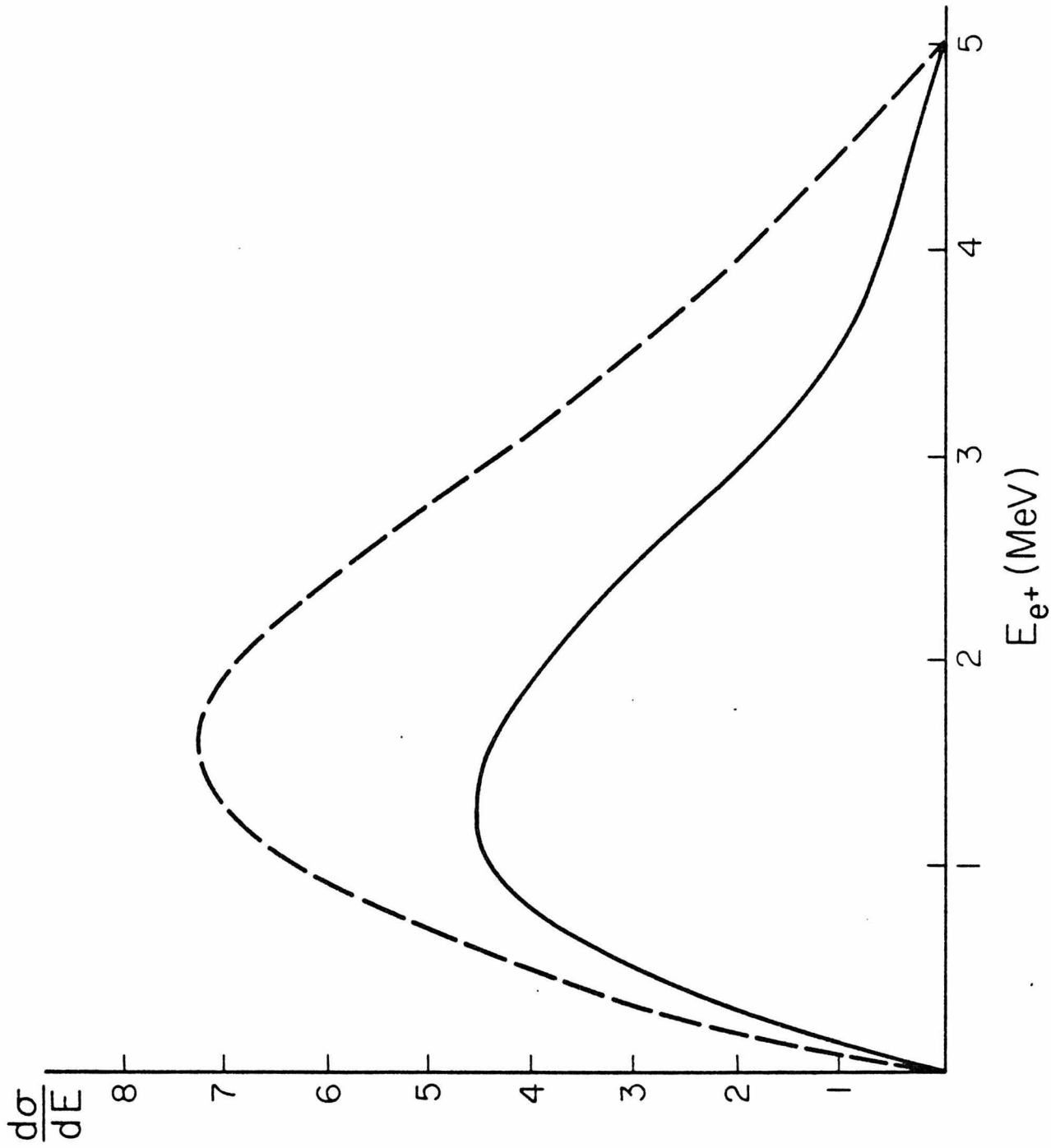

Fig. 8

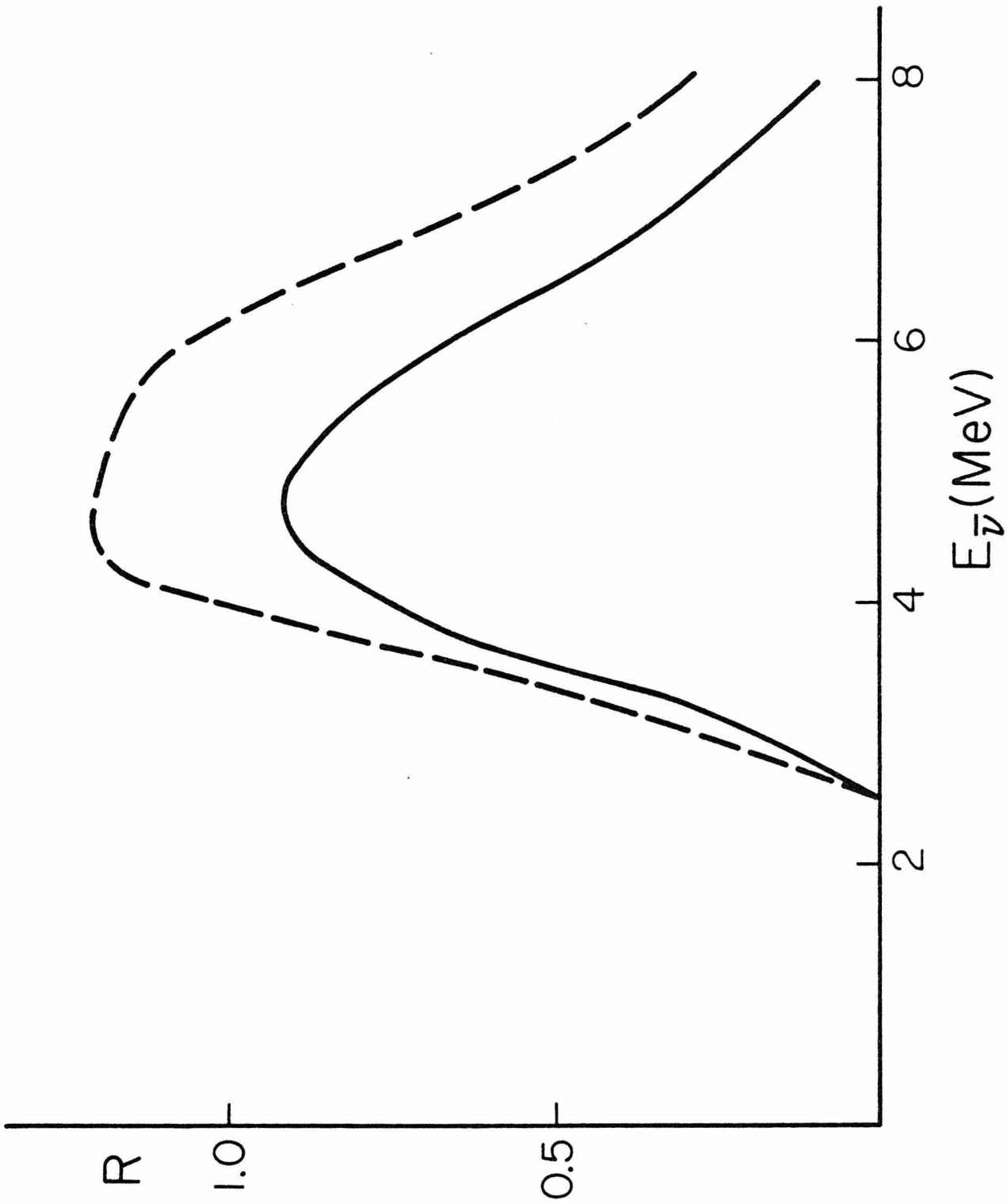

Fig. 9

PART II

ATOMIC FINAL STATE EFFECTS IN TESTS OF T-VIOLATION

CHAPTER 3

TIME REVERSAL TESTS IN NUCLEAR TRANSITIONS

TIME REVERSAL TESTS IN NUCLEAR TRANSITIONS

1. INTRODUCTION

Present studies of fundamental physics are deeply rooted in the identification and application of invariance principles. These principles reflect whether the laws describing a physical system are changed by the continuous or discrete transformation of certain variables or fields. In this section we discuss the discrete transformation of time-reversal and, in particular, its application to electro magnetic transitions in nuclear systems.

Gimlett *et al.*[1] have recently reported the measurement of a non-zero phase shift in the 129 keV mixed E2-M1 transition in ^{191}Ir. The observed value was in significant disagreement with the phase expected from atomic effects as calculated by Goldwire and Hannon.[2] This discrepancy represented an apparent violation of time-reversal invariance. A calculation of Davis, Koonin, and Vogel,[3] presented as Chapter 4 of this thesis, has since removed this disagreement; however, we wish to consider whether the magnitude of the apparent violation (at the level of 1×10^{-3} in the phase) was inconsistent with other tests of time-reversal invariance.

We conclude that the correlation experiment referred to above, does in fact represent a highly sensitive test of time-reversal invariance at levels not ruled out by other evidence. Thus, an accurate treatment of the atomic interference effects, discussed in the next chapter, is a necessary complement of the experimental efforts to search for T-violation in nuclear systems.

2. EXPERIMENTAL LIMITS ON TIME-REVERSAL VIOLATION

The only observation of time-reversal violation in a fundamental interaction was made in the neutral kaon system.[4] This experimental result is independent of the reported CP violation,[5] although the two are assumed to be related by the CPT theorem. Various theories have been proposed to explain these violations of CP and T at the observed level of 10^{-3}.[6] Included are the superweak and milliweak interactions, which have strengths 10^{-9} and 10^{-3} of the weak interaction strength, respectively; also postulated are the millistrong, and electromagnetic T-violating interactions, with strengths 10^{-4} and 10^{-4} - 10^{-3} relative to the strong force, respectively. We will briefly discuss later the expected effect of these theories for T-violation in nuclei.

Experimental studies of the neutron electric dipole moment, d_n, provide seemingly stringent upper limits on T-violation. Both parity and time-reversal need to be violated in order for d_n to be non-zero. Using a simple dimensional argument for the expected magnitude of the electric dipole moment,[7] we have:

$$d_n \simeq g_{TV}\, g_{PV}\, e\, \lambda\!\!\!^{-}, \qquad (1)$$

where g_{TV} and g_{PV} are the strengths for T- and P- violation relative to the strong interaction, e is the electron charge, and $\lambda\!\!\!^{-}$ is the Compton wave-length of the neutron. With $g_{PV} \sim 10^{-6}$ and the experimental upper limit, $d_n < 2 \times 10^{-24}$ e cm, one obtains $g_{TV} \leq 10^{-4}$. Thus, the existing

limits on d_n are not all that stringent, because they allow violation of time-reversal invariance at the level of about 10^{-4}.

The search for violation of time-reversal in nuclear systems has been conducted in a variety of investigations. We only enumerate them here; however, more detailed information may be found in a review article by Henley:[8] a) weak interaction tests, b) polarization tests in elastic scattering experiments, c) reciprocity or detailed-balance experiments, d) nuclear structure tests, and e) electromagnetic tests. The most stringent limits on T-violation in nuclei come from both detailed-balance and electromagnetic transition investigations. They provide, under certain assumptions, an upper limit of $\sim 3 \times 10^{-3}$ on the fractional violation of the strong-interactions strength.

3. IMPLICATIONS FOR TIME-REVERSAL TESTS IN NUCLEAR ELECTROMAGNETIC TRANSITIONS

The correlation experiments performed at CalTech and elsewhere, seek to observe a non-zero phase shift between the reduced matrix elements of individual multipoles in a mixed nuclear transition. This is equivalent to a complex multipole mixing ratio δ. A measurement of a non-zero phase shift, which could not be totally attributed to atomic effects, would be evidence for violation of time-reversal invariance. This violation could possibly originate in either the nuclear Hamiltonian which determines the energy eigen-states (causing them not to be T-eigen-states), or in the electromagnetic Hamiltonian responsible for the emission of the radiation.

To explore this further, we consider a simple three-state system[7] in which there is a mixed multipole ($L\pi$ and $L'\pi'$) de-excitation of initial state $|a>$ into final state $|f>$. We assume that state $|a>$ is mixed with a close-lying state $|b>$ by a time-reversal violating potential V_{TV}. The new state $|a'>$ is, by the application of perturbation theory:

$$|a'> = |a> + |b> \frac{<b|V_{TV}|a>}{\Delta E} , \tag{2}$$

where $\Delta E = E_a - E_b$. It is also assumed that the multipole operators, which act between the nuclear states, can have both T-conserving, $Q(L\pi)$, and T-violating, $Q_{TV}(L\pi)$, contributions. Then the transition mixing ratio δ can be written:

$$\delta = \frac{<f|Q(L\pi) + Q_{TV}(L\pi)|a'>}{<f|Q(L'\pi') + Q_{TV}(L'\pi')|a'>} \tag{3a}$$

$$\equiv |\delta| \; e^{i[\eta(L\pi) - \eta(L'\pi')]} . \tag{3b}$$

If we define $|\delta|$ to be:

$$|\delta| = \frac{<f|Q(L\pi)|a>}{<f|Q(L'\pi')|a>} , \tag{4}$$

we obtain the following expression for $\eta(L\pi)$:

$$\eta(L\pi) = \text{Im} \left\{ \frac{\langle f|Q_{TV}(L\pi)|a\rangle}{\langle f|Q(L\pi)|a\rangle} + \frac{\langle f|Q(L\pi)|b\rangle}{\langle f|Q(L\pi)|a\rangle} \frac{\langle b|V_{TV}|a\rangle}{\Delta E} \right\}, \tag{5}$$

where the matrix elements of Q_{TV} and V_{TV} are pure imaginary. A similar expression holds for $\eta(L'\pi')$.

In Eq. (5), we identify contributions to the phase $\eta(L\pi)$ from the T-violating parts of both the electromagnetic and nuclear Hamiltonians. One also observes the difficulty in establishing a direct connection between the measured quantity, $\sin\eta \approx \eta(L\pi) - \eta(L'\pi')$, and the T-violating strengths parameterizing Q_{TV} and V_{TV}. If one arbitrarily excludes the possibility of T-violation in the electromagnetic Hamiltonian, then enhancement effects can be achieved by seeking transitions where ΔE is very small and $\langle f|Q(L\pi)|a\rangle \ll \langle f|Q(L\pi)|b\rangle$.

There have been limited attempts to calculate the matrix element $\langle b|V_{TV}|a\rangle$ of a simple T-violating potential between close-lying states. For example, the effective interaction has taken the following form:

$$V_{TV} = G_{TV} \sum \frac{1}{2} (\vec{r}_i \cdot \vec{p}_i + \vec{p}_i \cdot \vec{r}_i), \tag{6}$$

where $\vec{r}_i$ is the position and $\vec{p}_i$ is the momentum of the i^{th} nucleon. Trial nuclear wave functions have been substituted for $|a\rangle$ and $|b\rangle$, and the integration performed. Such attempts have only been partially successful in relating G_{TV} to $\sin\eta$. However, crude estimates would predict an amplitude of the T-odd part in the nuclear wave functions

of the order 10^{-3}, 10^{-3}, 10^{-7} - 10^{-3}, and 10^{-9} for the T-violating millistrong, electromagnetic, milliweak, and superweak interactions, respectively.[9]

4. CONCLUSION

At the present time there is no definite relation between the strength of a time-reversal violating interaction and the phase shift measured at the level of 10^{-3}- 10^{-4}. However, if one makes the simple assumption that the measured sin η is of the same magnitude as the T-odd admixture in the nuclear wave function, then the correlation experiments are sensitive to predicted magnitudes of T-violation, except those given by the superweak theory. Such evidence would not be in striking contradiction to present experimental limits. Moreover, the sensitivity of these measurements permits them to be competitive with experiments on the neutron dipole moment in the search for time-reversal violation.

REFERENCES

[1]J. L. Gimlett, H. E. Henrikson, N. K. Cheung, and F. Boehm, Phys. Rev. Lett. 42, 354 (1979).

[2]H. C. Goldwire, Jr., and J. P. Hannon, Phys. Rev. B 16, 1875 (1977).

[3]B. R. Davis, S. E. Koonin, and P. Vogel, California Institute of Technology, Preprint (1980).

[4]R. C. Casella, Phys. Rev. Lett. 21, 1128 (1968); 22, 554 (1969).

[5]J. H. Christenson, J. W. Cronin, V. L. Fitch, and R. Turlay, Phys. Rev. Lett. 13, 138 (1964).

[6]K. Kleinknecht, Ann. Rev. Nucl. Sci. 26, 1 (1976).

[7]F. Boehm, private communication.

[8]E. M. Henley, Ann. Rev. Nucl. Sci. 19, 367 (1969).

[9]A. Richter, in Symposium on Interaction Studies in Nuclei, Proceedings of the 1975 Mainz Symposium, edited by H. Jachim and B. Ziegler (North Holland, Amsterdam, 1975).

CHAPTER 4

ATOMIC SCREENING OF NUCLEAR TRANSITIONS

This Chapter, with few modifications, will be submitted to Physical Review A for publication.

ATOMIC SCREENING OF NUCLEAR TRANSITIONS

B. R. DAVIS and S. E. KOONIN
W. K. Kellogg Radiation Laboratory
California Institute of Technology, Pasadena, California 91125

and

P. VOGEL
Department of Physics
California Institute of Technology, Pasadena, California 91125

ABSTRACT

In the analysis of Time-Reversal and Mössbauer Absorption Experiments, it is important to consider atomic processes which interfere with the direct nuclear transitions. Interaction of the photon with the atomic electrons causes the radiation to acquire a phase shift, specified by the interference parameter $\xi(L\pi)$. We present theoretical expressions for ξ, and compare our calculated values with experiment. Satisfactory agreement is obtained. In particular, an apparent violation of time-reversal invariance in the 129 keV transition of ^{191}Ir is fully explained by these effects.

1. INTRODUCTION

Photons emitted or absorbed in a nuclear transition may interact with the atomic electrons. Such processes will interfere with direct photon emission or absorption if the final states are indistinguishable from each other. In this paper, we consider processes which shift the photon phase by an amount of the order of the fine structure constant. This phase shift, $\xi(L, \pi = E \text{ or } M)$, depends upon both the multipolarity ($L\pi$) and the energy of the nuclear transition, and has been called the "screening" or "interference" parameter.[1-4]

There are two types of experiments for which a knowledge of ξ is important. The first of these tests time-reversal invariance in a mixed-multipole ($L\pi$ and $L'\pi'$) electromagnetic decay of an excited nucleus. One seeks to measure a relative phase between the transition matrix elements of the two competing multipoles. This phase, $\eta \equiv \eta(L\pi) - \eta(L'\pi')$, makes the mixing ratio δ complex:

$$\delta = \pm |\delta| e^{i\eta} \quad . \tag{1}$$

A nonvanishing value of η would be evidence for time-reversal violation.[5] However, the mixing ratio can acquire a spurious phase resembling η through the interaction of the radiated photon with the surrounding atomic electrons. This process, also sometimes called the "final state interaction", is shown schematically in Fig. 1. Diagram a) represents the amplitude for direct emission of a photon of multipolarity ($L\pi$) as the nucleus changes from initial state i to final state f. We denote this transition amplitude as $T_{fi}(L\pi)$. Diagrams b) and c) portray the elastic interaction of the photon with each of the bound electrons; they differ only in the relative time ordering. The initial and final state "o" of the electron are identical, with the photon

again emitted with multipolarity ($L\pi$). The nuclear radiation induces currents in the atomic electrons, which then also radiate. The sum of the transition amplitudes for graphs b) and c) is denoted by $\delta T_{fi}(L\pi)$, and, as will be shown later, the total transition amplitude for the de-excitation may be written as:

$$T_{fi}(L\pi) + \delta T_{fi}(L\pi) = T_{fi}(L\pi) \left\{ 1 + \rho(L\pi) + i\xi(L\pi) \right\} \qquad (2a)$$

$$\approx T_{fi}(L\pi)\, e^{i\xi(L\pi)} \quad , \qquad (2b)$$

with both ρ and $\xi \ll 1$. This modifies the observed mixing ratio for the transition to:

$$\delta = \pm |\delta|\, e^{i(\eta+\xi)} \quad , \qquad (3)$$

with $\xi = \xi(L\pi) - \xi(L'\pi')$, so that the relative phase measured in these experiments is actually $\eta + \xi$. Consequently, the knowledge of the interference parameter ξ is essential for determining the true magnitude of the time-reversal violation, η.

Gimlett et al.[6] have recently measured $\eta + \xi = (-4.7 \pm 0.3) \times 10^{-3}$ for the 129.5 keV E2-M1 transition in ^{191}Ir. Their result is to be compared with the theoretical value $\xi = -3.7 \times 10^{-3}$ calculated by Goldwire and Hannon,[1] including an estimate of the M-shell contributions. This significant discrepancy between experiment and theory, or in other words an apparent evidence for time-reversal violation, was the primary motivation for the present work.

The parameter ξ is also important for measurements of dispersion in Mössbauer absorption spectra. In transmission experiments, the total attenuation of the beam is due to the absorptive parts of scattering diagrams a) through d) in Fig. 2. Diagram a) shows the direct nuclear resonant scattering, diagrams b) and c) represent the interaction of the radiation with atomic electrons either preceding or following the nuclear resonant scattering,

and diagram d) shows direct scattering of photons by the electrons. Using the optical theorem, one can verify that the interference between the nuclear resonant absorption and the interaction with the atomic electrons yields an attenuation cross section:

$$\sigma = \frac{\sigma_o(1 - 2\xi x)}{1 + x^2} + \sigma_e \qquad (4)$$

where σ_o is the nuclear absorption cross section on resonance, and x is the deviation of the photon energy from the resonance energy in units of the transition half width. The quantity σ_e is the slowly varying total cross section for photoelectric absorption and elastic plus inelastic scattering from atomic electrons.

Equation (4) shows that the interference parameter produces an asymmetry in the absorption line shape. Such an asymmetry was first observed by Sauer, Matthias, and Mössbauer,[7] and has been treated theoretically by Trammell and Hannon[2,3] and Kagan et al.[8] It is also possible to measure contributions to the interference parameter by observing either ejected electrons (which reflect interference between photoelectrons and conversion electrons) or scattered x-rays (which reflect interference between resonant scattering from the nucleus and nonresonant scattering from the electrons). In comparing calculated and measured values of ξ for these experiments, it is necessary to properly take into account the effect of absorber thickness. This will be discussed in more detail below.

As pointed out earlier, the primary motivation of our present study was the apparent time-reversal violation observed by Gimlett et al.[6] We have rederived the formulas for the phase shift without approximations, particularly for the scattering part of ξ. Our numerical calculation is also more careful than that of Ref. 1; in particular, we use the more precise Hartree-Fock

treatment of the bound and continuum electron wave functions. The more accurate handling of the electron wave functions enabled us to extend the calculations of ξ to low energies, inaccessible in Ref. 1. It is at these low energy nuclear transitions where many of the precise Mössbauer type measurements of ξ are conducted. In addition, our exact treatment of the scattering part of ξ is applicable at energies well above 200 keV, where atomic interference effects least obscure any possible time-reversal violation. In general, we find very good agreement with experiment, not only for the 129.5 keV transition in ^{191}Ir where our calculated phase shift fully explains the observations,[6] but also in numerous Mössbauer type transitions.

In Sec. 2 we present theoretical expressions for the interference parameter ξ. A description of our calculation together with numerical results is given in Sec. 3. We compare our results for ξ with several Time-Reversal Violation and Mössbauer Absorption experiments in Sec. 4. The Appendix outlines the derivation of the formulas presented in Sec. 2.

2. EXPRESSIONS FOR THE INTERFERENCE PARAMETER

We begin by considering the contribution to the amplitude for nuclear de-excitation by diagrams a) through c) in Fig. 1. The direct emission of a photon of wave vector $\underset{\sim}{k}$, frequency $\omega = |\underset{\sim}{k}|$, normalization A, and polarization $\underset{\sim}{\varepsilon}$ induced by interaction with the nuclear electromagnetic transition current $\underset{\sim}{j}_n(\underset{\sim}{x})$ is:

$$T_{fi} = 2\pi i \int d\underset{\sim}{x}\, \underset{\sim}{j}_n(\underset{\sim}{x})\cdot A\, \underset{\sim}{\varepsilon}\, e^{-i\underset{\sim}{k}\cdot\underset{\sim}{x}} \quad , \tag{5}$$

where i and f are the initial and final states of the nucleus respectively, and $\omega = E_i - E_f$ is the energy of the transition.

We represent the sum of diagrams b) and c) as δT_{fi}, where in order for the processes to be indistinguishable from direct emission, the initial and final electron bound states are identical and the emitted photon is still described as above. Thus,

$$\delta T_{fi} = 2\pi i \int \underset{\sim}{dx}\underset{\sim}{dy} \frac{1}{4\pi} \frac{e^{i\omega|\underset{\sim}{y}-\underset{\sim}{x}|}}{|\underset{\sim}{y}-\underset{\sim}{x}|} \{\underset{\sim}{j}_n(\underset{\sim}{x})\cdot\underset{\sim}{j}_e(\underset{\sim}{y}) - \rho_n(\underset{\sim}{x})\ \rho_e(\underset{\sim}{y})\} \ . \qquad (6)$$

The electron current and density are defined as:

$$\begin{aligned}
\underset{\sim}{j}_e(\underset{\sim}{y},\omega) = \sum_o \{&-e^2 A \int \underset{\sim}{dz}\ \varphi_o^*(\underset{\sim}{z}) e^{-i\underset{\sim}{k}\cdot\underset{\sim}{z}}\ \underset{\sim}{\varepsilon}\cdot\underset{\sim}{\alpha}\ G_{E_o+\omega}(\underset{\sim}{z},\underset{\sim}{y})\ \underset{\sim}{\alpha}\varphi_o(\underset{\sim}{y}) \\
&-e^2 A \int \underset{\sim}{dz}\ \varphi_o^*(\underset{\sim}{y})\underset{\sim}{\alpha}\ G_{E_o-\omega}(\underset{\sim}{y},\underset{\sim}{z})\ e^{-i\underset{\sim}{k}\cdot\underset{\sim}{z}}\ \underset{\sim}{\varepsilon}\cdot\underset{\sim}{\alpha}\ \varphi_o(\underset{\sim}{z})\} \ , \\
\rho_e(\underset{\sim}{y},\omega) = \sum_o \{&-e^2\ A \int \underset{\sim}{dz}\ \varphi_o^*(\underset{\sim}{z}) e^{-i\underset{\sim}{k}\cdot\underset{\sim}{z}}\ \underset{\sim}{\varepsilon}\cdot\underset{\sim}{\alpha}\ G_{E_o+\omega}(\underset{\sim}{z},\underset{\sim}{y})\ \varphi_o(\underset{\sim}{y}) \\
&-e^2\ A \int \underset{\sim}{dz}\ \varphi_o^*(\underset{\sim}{y})\ G_{E_o-\omega}(\underset{\sim}{y},\underset{\sim}{z})\ e^{-i\underset{\sim}{k}\cdot\underset{\sim}{z}}\ \underset{\sim}{\varepsilon}\cdot\underset{\sim}{\alpha}\ \varphi_o(\underset{\sim}{z})\} \ .
\end{aligned} \qquad (7)$$

Here the summation is over all bound electron wave functions φ_o which satisfy the Dirac equation $(\underset{\sim}{\alpha}\cdot\underset{\sim}{p} + \beta m + eV(\underset{\sim}{r}))\varphi_o(\underset{\sim}{r}) = E_o\ \varphi_o(\underset{\sim}{r})$. The electron charge is e, $G_{E_o\pm\omega}$ is the electron Green's function of energy $E_o\pm\omega$ in the potential $V(\underset{\sim}{r})$ of the nucleus and the remaining electrons, and $\rho_n(\underset{\sim}{x})$ is the nuclear electromagnetic transition density. Equation (6) expresses δT_{fi} in a form very similar to that of internal conversion, but with $\underset{\sim}{j}_e$ and ρ_e taking on more complicated expressions.

In the Appendix we outline the multipole decomposition of the photon plane wave and Green's function, and the construction of the electron propagators $G_{E_o\pm\omega}$. The total transition amplitude $T_{fi} + \delta T_{fi}$ can be written as a sum of amplitudes for the emission of photons of specific multipolarities:

$$T_{fi} + \delta T_{fi} = \sum_{L,\pi} [T_{fi} + \delta T_{fi}]_{L,\pi} \ , \qquad (8)$$

where for the magnetic case we obtain

$$[T_{fi} + \delta T_{fi}]_{L,\,mag.} = \sum_M 2\pi i \left\{ \int d\underset{\sim}{x}\; \underset{\sim}{j}_n(\underset{\sim}{x}) \cdot \underset{\sim}{a}^{(o)*}_{LM}(\underset{\sim}{x}) \right\} \times \left\{ A(\underset{\sim}{\varepsilon} \cdot \underset{\sim}{Y}^{(o)}_{LM}(\hat{k})) + \frac{i\omega}{16\pi^2} \int d\underset{\sim}{y}\; \underset{\sim}{j}_e(\underset{\sim}{y}) \cdot \underset{\sim}{b}^{(o)}_{LM}(\underset{\sim}{y}) \right\} \tag{9}$$

and for the electric case:

$$[T_{fi} + \delta T_{fi}]_{L,\,elec.} = \sum_M 2\pi i \left\{ \int d\underset{\sim}{x}\; \underset{\sim}{j}_n(\underset{\sim}{x}) \cdot \underset{\sim}{a}^{(1)*}_{LM}(\underset{\sim}{x}) \right\} \times \left\{ A(\underset{\sim}{\varepsilon} \cdot \underset{\sim}{Y}^{(1)}_{LM}(\hat{k})) + \frac{i\omega}{16\pi^2} \int d\underset{\sim}{y} \left(\underset{\sim}{j}_e(\underset{\sim}{y}) \cdot \underset{\sim}{b}^{(1)}_{LM}(\underset{\sim}{y}) + \left(\frac{L}{L+1}\right)^{\frac{1}{2}} \underset{\sim}{b}^{(-1)}_{LM}(\underset{\sim}{y}) - \rho_e(\underset{\sim}{y}) \left(\frac{L}{L+1}\right)^{\frac{1}{2}} \varphi_{LM}(\underset{\sim}{y}) \right) \right\} . \tag{10}$$

Here the $\underset{\sim}{Y}_{LM}$'s are the vector spherical harmonics, the $\underset{\sim}{a}_{LM}$'s and $\underset{\sim}{b}_{LM}$'s are the vector multipole fields, and the φ_{LM}'s are the scalar multipole fields as defined in Akhiezer and Berestetskii.[9] In Eq. (A14) we show that the total transition amplitude $T_{fi} + \delta T_{fi}$ for each multipolarity ($L\pi$) given in Eqs. (9) and (10) can be expressed as Eq. (2a). This defines ξ and ρ.

As is clear from Fig. 1 and Eqs. (7), we have only considered processes contributing to order e^2 in the amplitude. Neglecting even higher order diagrams is justified by the smallness of the fine structure constant. The parameter ρ is in general much less than one, and is of little significance because it occurs in the combination $1 + \rho$. In contrast, the interference parameter $\xi(L\pi)$, although small, plays an important role because of its imaginary character.

It has been shown previously[1] that $\xi(L\pi)$ is a sum of two terms: the conversion phase ξ_c and the scattering phase ξ_s. These imaginary parts of the transition amplitude arise from the singularities of the electron and photon Green's functions, respectively. We now discuss each of these con-

tributions in greater detail.

A. ξ_c — The Conversion Phase

The electron propagator has a singularity when its energy equals that of a bound or free energy eigenstate. As indicated in Eqs. (7), we evaluate the Green's function G for energies $E_o+\omega$ and $E_o-\omega$, where E_o is the energy of each bound electron. For the transition energies which we consider here ($\omega < 2m$), pair production is forbidden and only $E_o+\omega$ can coincide with the energy of a continuum eigenstate. This is by definition when $E_o+\omega$ is greater than the electron rest mass. Note that we neglect terms where $E_o+\omega$ coincides exactly with an unoccupied bound state. Thus, the only contributions to the conversion phase come from diagram b) of Fig. 1. This is shown schematically in Fig. 3a), suggesting that ξ_c may be written as a product of two electron matrix elements: internal conversion followed by the inverse photoeffect. As is well known, the process of internal conversion is strongly energy dependent with those states just above threshold of greatest importance. We expect this same behavior for the conversion phase.

We define the solutions of the Dirac equation for the combined nuclear and atomic potential to be:

$$\varphi_o(\underset{\sim}{y}) = \frac{1}{y} \begin{pmatrix} g_{\kappa_o}(y)\, \chi_{\kappa_o \mu_o}(\hat{y}) \\ i f_{\kappa_o}(y)\, \chi_{-\kappa_o \mu_o}(\hat{y}) \end{pmatrix} , \qquad (11)$$

where g_{κ_o} and f_{κ_o} are the regular solutions to the radial Dirac equation:

$$\frac{dg_{\kappa_o}}{dy} + \frac{\kappa_o}{y} g_{\kappa_o} = + (E_o + m - eV(y)) f_{\kappa_o} \quad ,$$

$$\frac{df_{\kappa_o}}{dy} - \frac{\kappa_o}{y} f_{\kappa_o} = - (E_o - m - eV(y)) g_{\kappa_o} \quad , \tag{12}$$

and the χ's are angular momentum spinors with kappa of $\pm \kappa_o$, total angular momentum given by $|\kappa_o| - \frac{1}{2}$, and magnetic quantum number μ_o.

For the magnetic multipoles, the conversion phase can be written as:

$$\xi_c(L, \pi = \text{mag.}) = - \sum_{\kappa_o, \kappa} A_{\kappa_o \kappa}(m) \times R_{\kappa_o \kappa}(m) \times S_{\kappa_o \kappa}(m) \quad , \tag{13}$$

where the summation over κ_o includes all fully occupied subshells (the role of valence electrons is not significant for this problem), and the summation over κ represents all the final continuum states which are accessible to the initial state by the multipole selection rules. The other quantities appearing in Eq. (13) are:

$$A_{\kappa_o \kappa}(m) = \pi \alpha \omega \frac{1}{L(L+1)} (\kappa + \kappa_o)^2 (2j+1)(2j_o+1) \begin{pmatrix} j_o & j & L \\ \frac{1}{2} & -\frac{1}{2} & 0 \end{pmatrix}^2 \quad ,$$

$$R_{\kappa_o \kappa}(m) = \int_0^\infty dr \; y_L(\omega r) \{ f_\kappa g_{\kappa_o} + g_\kappa f_{\kappa_o} \} \quad , \tag{14}$$

$$S_{\kappa_o \kappa}(m) = \int_0^\infty dr \; j_L(\omega r) \{ f_\kappa g_{\kappa_o} + g_\kappa f_{\kappa_o} \} \quad .$$

Here, $\alpha = e^2/4\pi$ is the fine structure constant, j_L and y_L are the regular and irregular spherical Bessel functions, j_o and j are the angular momenta for the initial and final electron states respectively, f_{κ_o} and g_{κ_o} are the bound state radial wave functions, and f_κ, g_κ are the continuum wave functions which are regular at the origin. The normalization of the continuum states is defined in Eqs. (A9) of the Appendix. For comparison, the internal conversion coeffi-

cient is given by Rösel et al.[10] as

$$\alpha_m = \sum_{\kappa_o,\kappa} A_{\kappa_o\kappa}(m)\,\{R^2_{\kappa_o\kappa}(m) + S^2_{\kappa_o\kappa}(m)\} \quad . \tag{15}$$

Similarly, for electric transitions one obtains:

$$\xi_c(L,\pi = \text{elec.}) = -\sum_{\kappa_o,\kappa} A_{\kappa_o\kappa}(e) \times R_{\kappa_o\kappa}(e) \times S_{\kappa_o\kappa}(e) \tag{16}$$

where

$$\begin{aligned}
A_{\kappa_o\kappa}(e) &= \frac{1}{(\kappa+\kappa_o)^2} A_{\kappa_o\kappa}(m) \\
R_{\kappa_o\kappa}(e) &= \int_0^\infty dr\,\{-L\, y_L(\omega r)[g_{\kappa_o} g_\kappa + f_{\kappa_o} f_\kappa] \\
&\qquad -L\, y_{L-1}(\omega r)[f_{\kappa_o} g_\kappa - g_{\kappa_o} f_\kappa] \\
&\qquad + (\kappa-\kappa_o)\, y_{L-1}(\omega r)[f_{\kappa_o} g_\kappa + g_{\kappa_o} f_\kappa]\Big\} \\
S_{\kappa_o\kappa}(e)\left(\frac{L+1}{2L+1}\right) &\int_0^\infty dr\,\{-L\, j_{L+1}(\omega r)[f_{\kappa_o} g_\kappa - g_{\kappa_o} f_\kappa] \\
&\qquad -L\, j_{L-1}(\omega r)[f_{\kappa_o} g_\kappa - g_{\kappa_o} f_\kappa] \\
&\qquad -\frac{L}{L+1}(\kappa-\kappa_o)\, j_{L+1}(\omega r)[f_{\kappa_o} g_\kappa + g_{\kappa_o} f_\kappa] \\
&\qquad + (\kappa-\kappa_o)\, j_{L-1}(\omega r)[f_{\kappa_o} g_\kappa + g_{\kappa_o} f_\kappa]\} \quad .
\end{aligned} \tag{17}$$

The electric conversion coefficient is given by:

$$\alpha_e = \sum_{\kappa_o,\kappa} A_{\kappa_o\kappa}(e)\{R^2_{\kappa_o\kappa}(e) + S^2_{\kappa_o\kappa}(e)\} \tag{18}$$

which can again be shown to be equivalent to the expression in Ref. 10. In comparing our expression for the electric conversion phase with the formula of Hannon and Trammell,[4] we have found an apparent error in their result. Their Eqs. (19) or (21) should contain an additional factor of

$(L+1/2L+1)$. The formula for the electric conversion phase in the more recent paper Ref. 1 can be shown to be equivalent to our expression.

B. ξ_s — The Scattering Phase

This contribution to the imaginary part of the transition amplitude for photon emission occurs when the photon Green's function is singular. This corresponds to the photon being real as follows from the expression for the propagator:

$$\frac{\exp(i\omega|\underset{\sim}{y}-\underset{\sim}{x}|)}{|\underset{\sim}{y}-\underset{\sim}{x}|} = \frac{4\pi}{(2\pi)^3}\int d\underset{\sim}{q}\ \frac{\exp(i\underset{\sim}{q}\cdot(\underset{\sim}{y}-\underset{\sim}{x}))}{q^2-\omega^2-i\varepsilon} \quad . \tag{19}$$

Diagrams b) and c) of Fig. 3 show the emission of a real photon by the nucleus, which then scatters off all the bound atomic electrons. This scattering is elastic with the photon and electron states being unchanged by the interaction. The following expressions can be derived exactly using relativistic electron theory.

For the magnetic case we obtained:

$$\xi_s(L,\pi=\text{mag.}) = -2\sum_{\kappa_o,\kappa} A_{\kappa_o\kappa}(m)\times\left\{T_{\kappa_o\kappa}(E_o+\omega)+T_{\kappa_o\kappa}(E_o-\omega)\right\} \tag{20}$$

with

$$T_{\kappa_o\kappa} = \int_0^\infty dz\ \ j_L(\omega z)\{\bar{g}_\kappa f_{\kappa_o}+\bar{f}_\kappa g_{\kappa_o}\}_z \int_0^z dy\ j_L(\omega y)\{g_\kappa f_{\kappa_o}+f_\kappa g_{\kappa_o}\}_y \quad . \tag{21}$$

As before, κ_o labels the initial bound electron states, κ labels the intermediate states of energies $E_o+\omega$ and $E_o-\omega$ which can be connected to the initial state via the selection rules, and the subscript "y" or "z" denotes the argu-

ment of the radial wave functions. The intermediate electron states can either be continuum wave functions with energy greater than the electron mass or quasibound wave functions with energy less then the electron mass. $A_{\kappa_o\kappa}(m)$ is the angular factor given in Eq. (14), f_{κ_o} and g_{κ_o} are again the bound state wave functions, $\bar{f}_\kappa$ and $\bar{g}_\kappa$ are the wave functions which are irregular at the origin, and f_κ and g_κ are regular at the origin.

The analogous expression for the electric scattering phase is rather lengthy and is presented elsewhere.[11]

Goldwire and Hannon[1] have approximated the scattering phase as a sum of terms due to Thomson scattering (resulting from the A^2 interaction in the non-relativistic reduction) and anomalous scattering (arising from the $\underset{\sim}{j} \cdot \underset{\sim}{A}$ interaction). They claim that the Thomson term is dominant unless the transition is within a few eV of an absorption edge. We have found this to be true numerically even at higher energies where the approximation is no longer valid.

3. NUMERICAL RESULTS

In our calculations of the conversion and scattering phases, the potential V(r) was taken to be the appropriate Dirac-Hartree-Slater potential for each atom. The potential also included a simple correction for finite nuclear size. A fifth-order predictor-corrector integration method was used to solve the coupled differential Eqs. (12). The bound state eigenfunctions were obtained by choosing E_o so that two solutions matched at some intermediate radius: a regular one integrated outward from the origin and an exponentially decaying one, integrated inward from a very large radius.

For the continuum and quasi-bound wave functions, we integrated the regular function outward from the origin, normalized at a distant point, and then integrated inward to obtain the irregular wave function.

In Ref. 1, the conversion phases were calculated for the K and L shells only. Unscreened, point nucleus, relativistic wave functions were used for the K-shell, while a table of screened internal conversion matrix elements was employed for the L-shell. The Thomson contribution to the scattering phase in Ref. 1 was calculated using published relativistic radial densities.

The major part of the conversion phase comes from those innermost bound states above conversion threshold. The outer shells also contribute, but in a rapidly decreasing manner. This behavior is demonstrated in Fig. 4 where the contributions of various shells to the conversion phase for two representative transitions are graphed. The variation of the scattering phase with shell is much slower with no threshold behavior. We used the exact relativistic expression for those states providing most (70-90%) of the scattering phase. For the remaining states, we employed the much simpler Thomson approximation of Ref. 1. In Fig. 4 we display for the same transitions the contributions to the scattering phase for various atomic shells.

In general, our calculations agree with the conversion and scattering phases of Goldwire and Hannon.[1] However, there are instances of disagreement, particularly for some K-shell conversion phases. These must be considered in the comparison with experiments in Section 4 , particularly as regards the time-reversal violation test in ^{191}Ir.[6] Tables I-IV of Ref. 1 include nuclear transition energies up to 200 keV. Because both conversion and scattering phases decrease with increasing gamma energy, it may be desirable to perform Time-Reversal Experiments at higher energies. Therefore, we have calculated the phases at energies of 200, 500, and 800 keV,

and for nuclear charges 50, 70, and 90. Figures 5a), 5b), and 5c) present these results for E1, M1, and E2 type transitions respectively. These figures, together with Tables I-IV of Ref. 1, should give adequate estimates of ξ for any proposed experiments. However, in comparing theory with experiment, a more careful treatment of each transition is necessary. This is given in the next section for the existing experimental results.

There are several independent checks of our numerical work. These include comparisons with a) experimental electron binding energies, b) tabulated internal conversion coefficients, and c) experimental photoelectric cross sections.

a) Binding energies. A comparison of bound state energy eigenvalues tests both the quality of these wave functions, and that of the potential used to calculate the continuum and quasi-bound wave functions. The maximum difference we observed between the experimental and our calculated binding energies is of the order 1% for K-, L-, and M-shells. This comparison is quite satisfactory considering that higher-order effects such as virtual pair production are not included in the atomic potential.

b) Internal conversion coefficients. There is some similarity between the expressions for conversion phase and internal conversion coefficients, as will be noted in comparing Eqs. (13) and (15) or Eqs. (16) and (18). We have found that $R_{\kappa_o\kappa}$ is in general greater than $S_{\kappa_o\kappa}$ by two or three orders of magnitude in the region where the internal conversion coefficient and conversion phase are largest. Therefore, the internal conversion coefficient is effectively a measure of $R_{\kappa_o\kappa}$ in Eqs. (14) and (17). A comparison of our calculated coefficients with tabulated values strongly tests one factor in the conversion phase expression, and the results of this check are quite

satisfactory. Table 1 compares the total E1 internal conversion coefficients for the K, L, and M shells of selected 97.4 keV, 25.6 keV, and 6.21 keV transitions, respectively, with the tabulated values of Rösel et al.[10]

c) Photoelectric cross sections. As was mentioned in the discussion of the conversion phase, the second matrix element $S_{\kappa_o\kappa}$ is effectively the amplitude for photoelectric absorption of photons of multipolarity ($L\pi$). This can also be seen in equations (A1) and (A2) of Ref. 1 for absorption cross sections. In the energy region of interest, the experimental photoelectric cross section is dominated by the E1 contribution. Thus, by comparing our theoretical results for the photoelectric absorption cross section (calculated via the expressions of Ref. 1) with experimental data or extrapolated values,[12] we are only able to check the accuracy of $S_{\kappa_o\kappa}$ for E1 transitions. This comparison is presented for three selected E1 transitions in Table 4, showing our calculated values to lie within the quoted error bars. (We note that the E2 contribution to absorption, for the 97.4 keV transition, 1.04×10^2 barns/atom, was included in our calculated value.)

We estimate the uncertainty in our values for the interference parameter $\xi(L\pi)$ to be of the order of 1-2%. This takes into account, as best as possible, numerical aspects of the calculation and comparison with other relevant physical quantities. It must be noted, however, that due to subtraction there can be greater relative uncertainty in $\xi = \xi(L\pi) - \xi(L'\pi')$ measured in Time-Reversal Violation Experiments.

4. COMPARISON WITH EXPERIMENT

In this section we compare our calculated values for the interference parameter with results of both Time-Reversal Violation and Mössbauer Absorption Experiments. The computed phases ξ include both conversion and scattering contributions as described in the preceding section. The only difference is that the scattering phase for some outer electron states was calculated according to the approximate expressions (16) and (17) of Ref. 1. These formulae require substantially less time for numerical computation and, as remarked earlier, generally give values close to those resulting from the exact expressions.

In Table 2 we present the experimentally measured values of ξ together with their literature references. For Mössbauer experiments, it is necessary to correct the experimental results for absorber thickness. This effect, which causes the measured dispersion of absorption spectra to increase with absorber thickness, has been discussed by several authors; see, for example, Refs. 13-14. An extrapolation to zero thickness is required for accurate comparison with our values. This correction can be significant, as demonstrated by the phase ξ for the 6.21 keV E1 transition of $^{181}_{73}$Ta which was revised in Ref. 15 from the value $(-15.5 \pm 0.5) \times 10^{-2}$ given in Ref. 7 to $(-11 \pm 1) \times 10^{-2}$. A review of the literature has shown that most experimentalists have considered this effect and, when possible, corrected their values accordingly. A possible exception to this were Wagner et al.[16] who alleged that their use of absorbers of thickness $t \leq 2$ required no correction (where t is a dimensionless measure of thickness as defined, for example, in Ref. 14). However, finite thickness corrections to measurements performed at $t = 2$ can be as large as 50%.[14]

For transitions of mixed E2-M1 multipolarity, the relevant phase measured in Time-Reversal Experiments is $\xi = \xi(E2) - \xi(M1)$, and the phase determined by Mössbauer Experiments is $\xi = [\xi(M1) + \delta^2\ \xi(E2)]/(1 + \delta^2)$. We have used the mixing ratios δ given in the experimental references.

The agreement between calculated and measured values[6,14-24] is quite good as portrayed graphically in Figure 6. The largest discrepancies occur in the 46.5, 100.1, and 122.5 keV transitions of tungsten measured by Wagner et al.[16] Perhaps the failure to correct for non-zero thickness could explain the larger experimental values for the 100.1 and 122.5 keV transitions. Also, one would have expected that the measured phases for the 99.1 and 100.1 keV E2 transitions in tungsten to be nearly equal, as there are no threshold effects at this energy to cause such a difference. In both the 25.6 keV transition of ^{161}Dy and the 97.4 keV transition of ^{153}Eu we are in satisfactory agreement with one experimental result while differing significantly with the other. We include both measurements of each transition in Table II and Figure 6. For the majority of these transitions, our values are quite close to those of Ref. 1. Those authors, however, were unable to calculate the interference parameter for the lowest energy transition — the 6.21 keV line in tantalum. Our value for this Mössbauer transition is in excellent accord with experiment.

We have also computed phases arising from final state atomic effects in two recent Time-Reversal Violation Experiments. There is agreement with the 122.1 keV mixed E2-M1 transition in $^{57}_{26}$Fe,[24] and the experimental value for the 364.5 keV transition in xenon will be published in the near future,[25] indicating no violation of time-reversal at the level of the experimental uncertainty. We note that the near equality of E2 and M1 phases for the xenon transition causes the theoretical uncertainty ($.01 \times 10^{-2}$) to be the

same magnitude as the expected phase difference.

Of greatest significance is our agreement with the observed phase shift for the 129.5 keV transition of $^{191}_{77}$Ir. The calculated value of $(-4.3 \pm 0.4) \times 10^{-3}$ (the indicated error bars reflecting the 2% uncertainty in both E2 and M1 phases) shows no discrepancy with the experimental value of $(-4.7 \pm 0.3) \times 10^{-3}$.[6] This removes the apparent evidence for Time-Reversal Violation, which originated in a comparison with the values presented in Ref. 1. We differ with Goldwire and Hannon[1] primarily in the K-shell conversion phase for both multipolarities. Good agreement with binding energies and tabulated internal conversion coefficients for the K-shell verifies the accuracy of our calculation.

ACKNOWLEDGMENTS

We acknowledge helpful conversations with F. Boehm and J. Gimlett, and thank G. Wortman for alerting us to the affect of absorber thickness on Mössbauer Absorption Experiments. This work was supported in part by the National Science Foundation [PHY77-21602 and PHY79-23638] and the U.S. Department of Energy [DE AC-03-76-ER0063]. S. E. Koonin is an Alfred P. Sloan Foundation Research Fellow.

APPENDIX A

DERIVATION OF EXPRESSIONS FOR INTERFERENCE PARAMETER ξ

This appendix outlines the steps taken to obtain the formulas for conversion and scattering phases in Sec. 2. The method is in many respects similar to that used by Rose[26] in discussing the process of internal conversion. One initially performs a multipole decomposition of the photon plane wave and photon Green's function which occur in Eqs. (5) and (6) respectively:

$$\underset{\sim}{\varepsilon} e^{-i\underset{\sim}{k}\cdot\underset{\sim}{x}} = \sum_{L,M}\left\{\underset{\sim}{\varepsilon}\cdot\underset{\sim}{Y}^{(o)}_{LM}(\hat{k})\ \underset{\sim}{a}^{(o)*}_{LM}(\underset{\sim}{x}) + \underset{\sim}{\varepsilon}\cdot\underset{\sim}{Y}^{(1)}_{LM}(\hat{k})\ \underset{\sim}{a}^{(1)*}_{LM}(\underset{\sim}{x})\right\} \tag{A1}$$

$$\frac{e^{i\omega|\underset{\sim}{y}-\underset{\sim}{x}|}}{|\underset{\sim}{y}-\underset{\sim}{x}|}\ \underset{\sim}{j}_e(\underset{\sim}{y})\cdot\underset{\sim}{j}_n(\underset{\sim}{x}) = \frac{i\omega}{4\pi}\sum_{L,M,\,t=0,1,-1}\{\underset{\sim}{j}_n(\underset{\sim}{x})\cdot\underset{\sim}{a}^{(t)*}_{LM}(\underset{\sim}{x})\}\times\{\underset{\sim}{j}_e(\underset{\sim}{y})\cdot\underset{\sim}{b}^{(t)}_{LM}(\underset{\sim}{y})\} \tag{A2}$$

$$\frac{e^{i\omega|\underset{\sim}{y}-\underset{\sim}{x}|}}{|\underset{\sim}{y}-\underset{\sim}{x}|}\ \rho_e(\underset{\sim}{y})\ \rho_n(\underset{\sim}{x}) = 4\pi i\omega\sum_{L,M}\{\rho_n(\underset{\sim}{x})\ j_L(\omega x)\ Y^*_{LM}(\hat{x})\}\times\{\rho_e(\underset{\sim}{y})\ h_L(\omega y)\ Y_{LM}(\hat{y})\} \tag{A3}$$

The expansions in equations (A2) and (A3) are valid for $x < y$, where x and y are the magnitudes of position vectors $\underset{\sim}{x}$ and $\underset{\sim}{y}$ respectively. The $\underset{\sim}{Y}^{(o)}_{LM}$ and $\underset{\sim}{Y}^{(1)}_{LM}$ are vector spherical harmonics of magnetic and electric type, respectively, the $\underset{\sim}{a}^{(t)}_{LM}$'s and $\underset{\sim}{b}^{(t)}_{LM}$'s are the vector multipole fields of type magnetic, electric, and longitudinal for t = 0, 1, -1 respectively, as defined in Akhiezer and Berestetskii,[9] and the Y_{LM}'s are scalar spherical harmonics. These expressions lead immediately to the results for $T_{fi} + \delta T_{fi}$ given in Eqs. (9) and (10).

The other important element of the derivation involves construction of the Dirac propagator for the electron, which satisfies:

$$(E - \underset{\sim}{\alpha}\cdot\underset{\sim}{p} - \beta m - eV(\underset{\sim}{x}))\, G_E(\underset{\sim}{x},\underset{\sim}{y}) = I\delta(\underset{\sim}{x}-\underset{\sim}{y}) \quad , \tag{A4}$$

where I is the 4×4 unit matrix. We write $G_E(\underset{\sim}{x},\underset{\sim}{y})$ in the following form:

$$G_E(\underset{\sim}{x},\underset{\sim}{y}) = \sum_{\kappa,\mu} \frac{1}{xy} \begin{pmatrix} \chi_{\kappa\mu}(\hat{x})\ \chi^{+}_{\kappa\mu}(\hat{y})\ G_{++}(x,y) & -i\chi_{\kappa\mu}(\hat{x})\ \chi^{+}_{-\kappa\mu}(\hat{y})\ G_{+-}(x,y) \\ i\chi_{-\kappa\mu}(\hat{x})\ \chi^{+}_{\kappa\mu}(\hat{y})\ G_{-+}(x,y) & \chi_{-\kappa\mu}(\hat{x})\ \chi^{+}_{-\kappa\mu}(\hat{y})\ G_{--}(x,y) \end{pmatrix} , \tag{A5}$$

as is possible for a spherically-symmetric potential V(x). The radial Green's functions G_{++}, G_{+-}, G_{-+}, G_{--} depend on E and x (but not μ), and satisfy the following coupled differential equations:

$$\begin{aligned} &-(E - m - eV(x))G_{++} - (G'_{-+} - \tfrac{\kappa}{x} G_{-+}) = \delta(x-y) \\ &G'_{++} + \tfrac{\kappa}{x} G_{++} - (E + m - eV(x))G_{-+} = 0 \\ &-(E - m - eV(x))G_{+-} - (G'_{--} - \tfrac{\kappa}{x} G_{--}) = 0 \\ &G'_{+-} + \tfrac{\kappa}{x} G_{+-} - (E + m - eV(x))G_{--} = \delta(x-y) \quad . \end{aligned} \tag{A6}$$

Here the primes " ' " denote derivatives with respect to the variable x. For the energies relevant to our calculations (E > -m), these equations are solved by:

$$\begin{pmatrix} G_{++}(x,y) \\ G_{-+}(x,y) \\ G_{+-}(x,y) \\ G_{--}(x,y) \end{pmatrix} = \frac{1}{W} \left(\begin{array}{c|c} g_o(x)g_+(y) & g_+(x)g_o(y) \\ f_o(x)g_+(y) & f_+(x)g_o(y) \\ g_o(x)f_+(y) & g_+(x)f_o(y) \\ f_o(x)f_+(y) & f_+(x)f_o(y) \end{array}\right) \quad . \tag{A7}$$

$$x < y \qquad\qquad x > y$$

In the continuum case ($E > m$):

$$p = (E^2 - m^2)^{\frac{1}{2}}, \quad W = \frac{ip}{E+m} \tag{A8}$$

and the "large" radial wave functions g_o (regular), g_- (irregular), and g_+ (outgoing) solve equations (12) with the asymptotic forms as $y \to \infty$:

$$\begin{aligned} g_o &\sim \left(\frac{p(E+m)}{\pi}\right)^{\frac{1}{2}} y \quad \{\cos \delta' \, j_\ell(py) - \sin \delta' \, y_\ell(py)\} \\ g_- &\sim \left(\frac{p(E+m)}{\pi}\right)^{\frac{1}{2}} y \quad \{\sin \delta' \, j_\ell(py) + \cos \delta' \, y_\ell(py)\} \\ g_+ &= g_o + i g_- \quad . \end{aligned} \tag{A9}$$

The orbital angular momentum ℓ is given by:

$$\ell = \begin{cases} \kappa & \text{for} \quad \kappa > 0 \\ -\kappa - 1 & \text{for} \quad \kappa < 0 \end{cases} \quad . \tag{A10}$$

The parameter δ' is related to the conventional phase shift δ by $\delta' = \delta + \pi(\ell + 1)/2$. This latter phase is defined by the asymptotic form for the regular wave function g_o:

$$g_o \sim \left(\frac{E+m}{\pi p}\right)^{\frac{1}{2}} \cos (py + \delta) \quad . \tag{A11}$$

The asymptotic forms for the "small" radial functions f_o, f_-, f_+ are obtained from g_o, g_-, g_+ by the coupled differential equations (12) with the potential V set equal to zero. It is usual in atomic calculations to employ the asymptotic forms of the radial wave functions represented by Eq. (A11). However, this assumes that both the potential and centrifugal barrier are very small at the radius of normalization. In our case the centrifugal barrier was not in general negligible, and thus, we used these more appropriate asymptotic expressions (A9).

For the quasi-bound case ($-m < E < m$):

$$p = (m^2 - E^2)^{\frac{1}{2}} \quad , \qquad W = \frac{-p}{E+m} \tag{A12}$$

and the radial wave functions g_o (regular), and g_+ (irregular) have the asymptotic forms:

$$\begin{aligned} g_o &\sim \frac{e^{pr}}{2}\left\{1 - \frac{\kappa(\kappa+1)}{2}\cdot\frac{1}{pr} + \mathcal{O}\left(\left(\frac{1}{pr}\right)^2\right)\right. \\ g_+ &\sim \left(\frac{E+m}{\pi p}\right)^{\frac{1}{2}} e^{-pr}\left\{1 + \frac{\kappa(\kappa+1)}{2}\cdot\frac{1}{pr} + \mathcal{O}\left(\left(\frac{1}{pr}\right)^2\right)\right. \quad . \end{aligned} \tag{A13}$$

The "small" functions f_o and f_+ are obtained from g_o and g_+ as described above.

When the solutions for $G_E(\underset{\sim}{x},\underset{\sim}{y})$ given by Eqs. (A5) and (A7) are inserted into Eqs. (9) and (10), with the angular parts coupled correctly to those coming from the photon, the resulting expression for the magnetic case is:

$$\begin{aligned} &\left[T_{fi} + \delta T_{fi}\right]_{L,\,mag.} = \\ &\sum_M \left[2\pi i \left\{\int d\underset{\sim}{x}\; \underset{\sim}{j}_n(\underset{\sim}{x}) \cdot \underset{\sim}{a}^{(o)*}_{LM}(\underset{\sim}{x})\right\} \cdot A(\underset{\sim}{\varepsilon} \cdot \underset{\sim}{Y}^{(o)}_{LM}(\hat{k}))\right] \\ &\times \left\{1 - i \sum_{\kappa_o,\kappa} A_{\kappa_o\kappa}(m) \int_0^\infty dz \int_0^\infty dy\; h_L(\omega y)\; j_L(\omega z)\right. \\ &\quad \times \left\{\left[f_{\kappa_o}(z)\left\{f_{\kappa_o}(y)\, G^+_{++}(z,y) + g_{\kappa_o}(y)\, G^+_{+-}(z,y)\right\}\right.\right. \\ &\qquad + g_{\kappa_o}(z)\left\{f_{\kappa_o}(y)\, G^+_{-+}(z,y) + g_{\kappa_o}(y)\, G^+_{--}(z,y)\right\}\Big] \\ &\qquad + \left[f_{\kappa_o}(z)\left\{f_{\kappa_o}(y)\, G^-_{++}(y,z) + g_{\kappa_o}(y)\, G^-_{-+}(y,z)\right\}\right. \\ &\qquad \left.\left.\left. + g_{\kappa_o}(z)\left\{f_{\kappa_o}(y)\, G^-_{+-}(y,z) + g_{\kappa_o}(y)\, G^-_{--}(y,z)\right\}\right]\right\}\Bigg\} \quad . \end{aligned} \tag{A14}$$

The superscripts "+" or "-" on the G's refer to energies $E_o + \omega$ or $E_o - \omega$, respectively. The imaginary part of the above expression gives the magnetic

interference parameter $\xi(L\pi)$ as the sum of two parts: the conversion phase of Eq. (13) and the scattering phase of Eq. (20).

A similar procedure applies for the electric interference parameter; however, space does not permit the reproduction here of the lengthy scattering formula. The reader is referred to Ref. 11 for further details.

APPENDIX B

EXPRESSIONS FOR THE ELECTRIC SCATTERING PHASE ξ_S

This appendix contains the scattering phase for electric multipoles. It was derived using a procedure similar to that presented in Appendix A. We begin by defining $X_1 - X_5$ as:

$$X_1 = \int_o^z dy\ j_L(\omega y)\{g_{\kappa_o} g_\kappa + f_{\kappa_o} f_\kappa\}_y$$

$$X_2 = \int_o^z dy\ j_{L+1}(\omega y)\{f_{\kappa_o} g_\kappa + g_{\kappa_o} f_\kappa\}_y$$

$$X_3 = \int_o^z dy\ j_{L-1}(\omega y)\{f_{\kappa_o} g_\kappa + g_{\kappa_o} f_\kappa\}_y \qquad \text{(B1)}$$

$$X_4 = \int_o^z dy\ j_{L+1}(\omega y)\{f_{\kappa_o} g_\kappa - g_{\kappa_o} f_\kappa\}_y$$

$$X_5 = \int_o^z dy\ j_{L-1}(\omega y)\{f_{\kappa_o} g_\kappa - g_{\kappa_o} f_\kappa\}_y$$

As in Sect. 2 and Appendix A, κ_o labels the initial bound electron states, κ labels the intermediate states of energies $E_o + \omega$ and $E_o - \omega$ which can be connected to the initial state via the selection rules, and the subscript "y" denotes the argument of the radial wave functions. f_{κ_o} and g_{κ_o} are the bound state wave functions, and f_κ and g_κ are the wavefunctions which are regular at the origin.

We now proceed to introduce R_1-R_{20}:

$$
\begin{aligned}
R_1 &= \int_0^\infty dy\; j_{L+1}(\omega z)\{f_{\kappa_o}\bar{g}_\kappa - g_{\kappa_o}\bar{f}_\kappa\}_z\; X_{1z} & R_{11} &= \int_0^\infty dy\; j_{L-1}(\omega z)\{f_{\kappa_o}\bar{g}_\kappa - g_{\kappa_o}\bar{f}_\kappa\}_z\; X_{1z}\\
R_2 &= \int_0^\infty dy\; j_{L+1}(\omega z)\{f_{\kappa_o}\bar{g}_\kappa - g_{\kappa_o}\bar{f}_\kappa\}_z\; X_{5z} & R_{12} &= \int_0^\infty dy\; j_{L-1}(\omega z)\{f_{\kappa_o}\bar{g}_\kappa - g_{\kappa_o}\bar{f}_\kappa\}_z\; X_{5z}\\
R_3 &= \int_0^\infty dy\; j_{L+1}(\omega z)\{f_{\kappa_o}\bar{g}_\kappa - g_{\kappa_o}\bar{f}_\kappa\}_z\; X_{3z} & R_{13} &= \int_0^\infty dy\; j_{L-1}(\omega z)\{f_{\kappa_o}\bar{g}_\kappa - g_{\kappa_o}\bar{f}_\kappa\}_z\; X_{4z}\\
R_4 &= \int_0^\infty dy\; j_{L+1}(\omega z)\{f_{\kappa_o}\bar{g}_\kappa + g_{\kappa_o}\bar{f}_\kappa\}_z\; X_{1z} & R_{14} &= \int_0^\infty dy\; j_{L-1}(\omega z)\{f_{\kappa_o}\bar{g}_\kappa - g_{\kappa_o}\bar{f}_\kappa\}_z\; X_{2z}\\
R_5 &= \int_0^\infty dy\; j_{L+1}(\omega z)\{f_{\kappa_o}\bar{g}_\kappa + g_{\kappa_o}\bar{f}_\kappa\}_z\; X_{5z} & R_{15} &= \int_0^\infty dy\; j_{L-1}(\omega z)\{f_{\kappa_o}\bar{g}_\kappa - g_{\kappa_o}\bar{f}_\kappa\}_z\; X_{3z}\\
R_6 &= \int_0^\infty dy\; j_{L+1}(\omega z)\{f_{\kappa_o}\bar{g}_\kappa + g_{\kappa_o}\bar{f}_\kappa\}_z\; X_{3z} & R_{16} &= \int_0^\infty dy\; j_{L-1}(\omega z)\{f_{\kappa_o}\bar{g}_\kappa + g_{\kappa_o}\bar{f}_\kappa\}_z\; X_{1z}\\
R_7 &= \int_0^\infty dy\; j_{L}(\omega z)\{g_{\kappa_o}\bar{g}_\kappa + f_{\kappa_o}\bar{f}_\kappa\}_z\; X_{4z} & R_{17} &= \int_0^\infty dy\; j_{L-1}(\omega z)\{f_{\kappa_o}\bar{g}_\kappa + g_{\kappa_o}\bar{f}_\kappa\}_z\; X_{5z}\\
R_8 &= \int_0^\infty dy\; j_{L}(\omega z)\{g_{\kappa_o}\bar{g}_\kappa + f_{\kappa_o}\bar{f}_\kappa\}_z\; X_{5z} & R_{18} &= \int_0^\infty dy\; j_{L-1}(\omega z)\{f_{\kappa_o}\bar{g}_\kappa + g_{\kappa_o}\bar{f}_\kappa\}_z\; X_{4z}\\
R_9 &= \int_0^\infty dy\; j_{L}(\omega z)\{g_{\kappa_o}\bar{g}_\kappa + f_{\kappa_o}\bar{f}_\kappa\}_z\; X_{2z} & R_{19} &= \int_0^\infty dy\; j_{L-1}(\omega z)\{f_{\kappa_o}\bar{g}_\kappa + g_{\kappa_o}\bar{f}_\kappa\}_z\; X_{3z}\\
R_{10} &= \int_0^\infty dy\; j_{L}(\omega z)\{g_{\kappa_o}\bar{g}_\kappa + f_{\kappa_o}\bar{f}_\kappa\}_z\; X_{3z} & R_{20} &= \int_0^\infty dy\; j_{L-1}(\omega z)\{f_{\kappa_o}\bar{g}_\kappa + g_{\kappa_o}\bar{f}_\kappa\}_z\; X_{2z}
\end{aligned}
\tag{B2}
$$

Here the subscript "z" on the X's denotes the upper limit of the integral, and $\bar{f}_\kappa$ and $\bar{g}_\kappa$ are the wavefunctions which are irregular at the origin.

We now present our result from the electric scattering phase:

$$
\xi_S(L,\ \pi = \text{elec.}) = \sum_{\kappa_o,\kappa} A_{\kappa_o\kappa}(e)\left(\frac{L(L+1)}{2L+1}\right)\left\{U_{\kappa_o\kappa}(E_o+\omega) - V_{\kappa_o\kappa}(E_o-\omega)\right\},
\tag{B3}
$$

where $A_{\kappa_o\kappa}(e)$ was defined in Eq. (17) and $U_{\kappa_o\kappa}$, $V_{\kappa_o\kappa}$ are:

$$
\begin{aligned}
U_{\kappa_o\kappa} = \quad & -L\,(\,R_1 + R_2 + R_7 + R_8 + R_{11} + 2R_{12} + R_{13}\,) \\
& + (\kappa - \kappa_o)\,(\,R_3 + R_{10} + 2R_{15} + R_{16} + 2R_{17} + R_{18}\,) \\
& - (\,L\,(\kappa - \kappa_o)/(L+1))\,(\,R_4 + R_5 + R_9 + R_{14}\,) \\
& + ((\kappa - \kappa_o)^2)/(L+1)\,(\,R_6 + R_{20}) \\
& - ((\kappa - \kappa_o)^2)/L\,(2R_{19}\,) \quad ,
\end{aligned}
\tag{B4}
$$

$$
\begin{aligned}
V_{\kappa_o\kappa} = \quad & -L\,(-R_1 + R_2 - R_7 - R_8 - R_{11} + 2R_{12} + R_{13}\,) \\
& + (\kappa - \kappa_o)\,(\,R_3 - R_{10} + 2R_{15} - R_{16} + 2R_{17} + R_{18}\,) \\
& - (\,L\,(\,\kappa - \kappa_o)/(L+1))\,(-R_4 + R_5 - R_9 + R_{14}\,) \\
& + ((\kappa - \kappa_o)^2)/(L+1)\,(R_6 + R_{20}) \\
& - ((\kappa - \kappa_o)^2)/L\,(2R_{19}\,) \quad .
\end{aligned}
$$

REFERENCES

[1]H. C. Goldwire, Jr. and J. P. Hannon, Phys. Rev. B 16, 1875 (1977).

[2]J. P. Hannon and G. T. Trammell, Phys. Rev. Lett. 21, 726 (1968).

[3]G. T. Trammell and J. P. Hannon, Phys. Rev. 180, 337 (1969).

[4]J. P. Hannon and G. T. Trammell, Phys. Rev. 186, 306 (1969).

[5]S. P. Lloyd, Phys. Rev. 81, 161 (1951).

[6]J. L. Gimlett, H. E. Henrikson, N. K. Cheung, and F. Boehm, Phys. Rev. Lett. 42, 354 (1979).

[7]C. Sauer, E. Matthias, and R. L. Mössbauer, Phys. Rev. Lett. 21, 961 (1968).

[8]Yu. Kagan, A. M. Afanas'ev, and V. K. Voitovetskii, Zh. Eksp. Teor. Fiz. Pis'ma Red. 9, 155 (1969) [JETP Lett. 9, 91 (1969)].

[9]A. I. Akhiezer and V. B. Berestetskii, Quantum Electrodynamics (Wiley-Interscience Publishers, Inc., New York, 1965).

[10]F. Rösel, H. M. Fries, K. Alder, and H. C. Pauli, Atomic Data and Nuclear Data Tables 21, 91 (1978).

[11]B. R. Davis, Ph.D. thesis, California Institute of Technology, 1980 (unpublished).

[12]W. J. Veigele, Atomic Data 5, 51 (1973).

[13]B. T. Cleveland and J. Heberle, Phys. Lett. 40A, 13 (1972).

[14]P. West, Nucl. Instr. Meth. 101, 243 (1972).

[15]D. Salomon, P. J. West, and G. Weyer, Hyperfine Interactions 5, 61 (1977).

[16]F. E. Wagner, B. D. Dunlap, G. M. Kalvius, H. Schaller, R. Felscher, and H. Spieler, Phys. Rev. Lett. 28, 530 (1972).

[17]L. Asch, W. Potzel, G. M. Kalvius, J. C. Spirlet, and W. Müller, Hyperfine Interactions 5, 457 (1978).

[18]W. Henning, G. Bähre, and P. Kienle, Phys. Lett. B 31, 203 (1970).

[19]D. J. Erickson, J. F. Prince, and L. D. Roberts, Phys. Rev. C 8, 1916 (1973).

[20]L. Pfeiffer, Phys. Rev. Lett. 38, 862 (1967).

[21]O. C. Kistner, Phys. Rev. Lett. 19, 872 (1967).

[22]M. Atac, B. Chrisman, P. Debrunner, and H. Frauenfelder, Phys. Rev. Lett. 20, 691 (1968).

[23]W. Potzel, F. E. Wagner, G. M. Kalvius, L. Asch, J. C. Spirlet, and W. Müller, AIP Conference Proceedings No. 38, 77 (1977).

[24]N. K. Cheung, H. E. Henrikson, and F. Boehm, Phys. Rev. C 16, 2381 (1977).

[25]J. L. Gimlett, private communication.

[26]M. E. Rose, Multipole Fields (John Wiley & Sons, Inc., New York, 1955).

TABLE 1. Comparison of tabulated internal conversion coefficients and photoelectric absorption cross sections for selected E1 transitions with results of present calculation.

Nuclear Charge	Energy (keV)	α [a]	$\alpha_{TAB.}$ [b]	σ(b/atom) [c]	$\sigma_{TAB.}$(b/atom) [d]
63	97.4	α_K = 2.56(-1)	2.56(-1)	7.49(2)	(7.57 ± 0.38)(2)
66	25.6	α_L = 1.82(0)	1.83(0)	5.94(3)	(6.36 ± 0.64)(3)
73	6.21	α_M = 2.45(1)	2.55(1)	8.98(4)	(9.31 ± 0.93)(4)

[a] Calculated total conversion coefficients for first contributing shell. 2.56(-1) denotes 2.56×10^{-1}.

[b] Tabulated values from Ref. 10.

[c] Calculated cross section for photoelectric absorption.

[d] Tabulated values with uncertainties from Ref. 12.

TABLE 2. Comparison of experimental interference parameters ξ with results of present calculation.

Isotope	ω (keV)	Multipolarity	100 ξ[a]	100 $\xi_{EXPT.}$[b]	Ref.
$^{57}_{26}Fe$	122.1	M1 + 1.4%E2	ξ = -0.06	ξ = -0.03 ± 0.07	24
$^{73}_{32}Ge$	13.3	E2	-3.24	-4.7 ± 1.0	20
$^{99}_{44}Ru$	90.0	E2 + 37%M1	-0.60	-0.33 ± 0.32	16
			ξ = -0.57[c]	ξ = -0.43 ± 0.50	21
$^{131}_{54}Xe$	364.5	E2 + 4.6%M1	ξ = -0.01[c]	d	
$^{153}_{63}Eu$	97.4	E1	-2.03	-1.1 ± 0.3 -1.4 ± 0.3	18 14
$^{155}_{64}Gd$	86.5	E1	-2.48	-2.5 ± 0.5	18
	105.3	E1	-1.85	-1.8 ± 0.5	18
$^{161}_{66}Dy$	25.6	E1	-3.97	-3.5 ± 0.5 -3.2 ± 0.3	18 14
	74.5	E1	-3.40	-3.0 ± 0.5	18
$^{166}_{68}Er$	80.6	E2	-1.37	-1.60 ± 0.19	16
$^{170}_{70}Yb$	84.3	E2	-1.33	-1.70 ± 0.38	16
$^{171}_{70}Yb$	66.7	M1 + 49%E2	-0.75	-1.00 ± 0.14	16
$^{180}_{72}Hf$	93.3	E2	-1.27	-1.82 ± 0.48	16
$^{181}_{73}Ta$	6.21	E1	-12.3	-11.0 ± 1.0	15
$^{182}_{74}W$	100.1	E2	-1.22	-1.71 ± 0.14	16
$^{183}_{74}W$	99.1	E2	-1.22	-1.25 ± 0.17	16
	46.5	M1 + 0.6%E2	-0.28	-0.05 ± 0.06	16

(continued)

TABLE 2.(continued)

Isotope	ω (keV)	Multipolarity	100 ξ[a]	100 $\xi_{EXPT.}$[b]	Ref.
$^{184}_{74}W$	111.1	E2	-1.17	-1.53 ± 0.29	16
$^{186}_{74}W$	122.5	E2	-1.10	-2.09 ± 0.36	16
$^{186}_{76}Os$	137.2	E2	-1.02	-1.02 ± 0.25	16
$^{188}_{76}Os$	155.0	E2	-0.93	-1.51 ± 0.49	16
$^{191}_{77}Ir$	129.5	M1 + 14%E2	-0.69	-0.50 ± 0.12	16
			ξ = -0.43[c]	ξ = -0.47 ± 0.03	6
$^{193}_{77}Ir$	73.1	M1 + 31%E2	ξ = -0.12[c]	ξ = 0.11 ± 0.38	22
$^{195}_{78}Pt$	98.7	M1	-0.70	-1.1 ± 0.3	23
$^{197}_{79}Au$	77.3	M1 + 12.1%E2	-0.40	-0.414 ± 0.017	19
$^{236}_{92}U$	45.3	E2	+0.31	+0.25 ± 0.75	16
$^{237}_{93}Np$	59.6	E1	-3.18	-3.4 ± 0.2	17

[a]Calculated interference parameters ξ. Both conversion and scattering contributions included.

[b]Measured values of ξ, together with experimental references.

[c]For Time-Reversal Violation Experiments, $\xi = \xi(E2) - \xi(M1)$.

[d]Experimental value to be published in the near future.[25]

FIGURE CAPTIONS

FIG. 1. Diagrammatic contributions to the amplitude for photon emission in a nuclear transition. The external wavy lines represent the emitted photon and the internal lines indicate virtual photon exchange. The single straight lines represent the electron, and the double lines the nucleus.

FIG. 2. Diagrams contributing to the scattering of a photon by a Mössbauer nucleus and its atomic electrons.

FIG. 3. Contributions to the interference parameter ξ. Diagram a) represents the conversion contribution, and Diagrams b) and c) the scattering portion of the phase.

FIG. 4. Phase ξ for two representative E2 transitions in tungsten. Contributions of different electron shells are shown for the 46.5 keV and 122.5 keV transitions in Figures 4a) and 4b), respectively. Full histogram-conversion phase; dashed histogram-scattering phase.

FIG. 5. Phase ξ for transition energies between 200 and 800 keV in nuclei of charge 50, 70, and 90. Figures 5a), 5b), and 5c) present results of calculation for E1, M1, and E2 type transitions, respectively. Interference parameters for energies less than 200 keV may be found in Ref. 1. Full curve-conversion phase; dashed curve-scattering phase.

FIG. 6. Comparison of calculation with experiment for the Time-Reversal Violation and Mössbauer Absorption measurements listed in Table 2.

The energy of transition is plotted horizontally; the difference between the calculated and experimentally measured phase shifts ($\xi - \xi_{EXPT.}$), in units of 10^{-2}, is plotted vertically. The error bars include only those of the experiment.

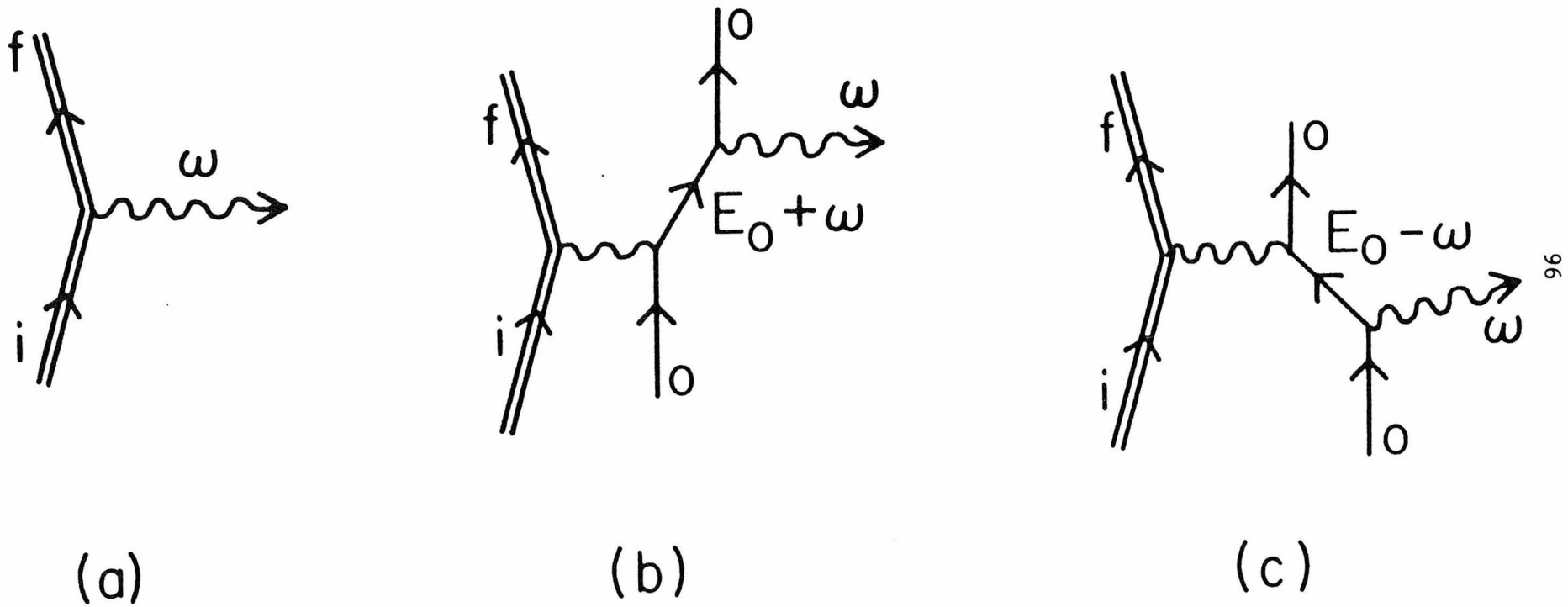

Fig. 1

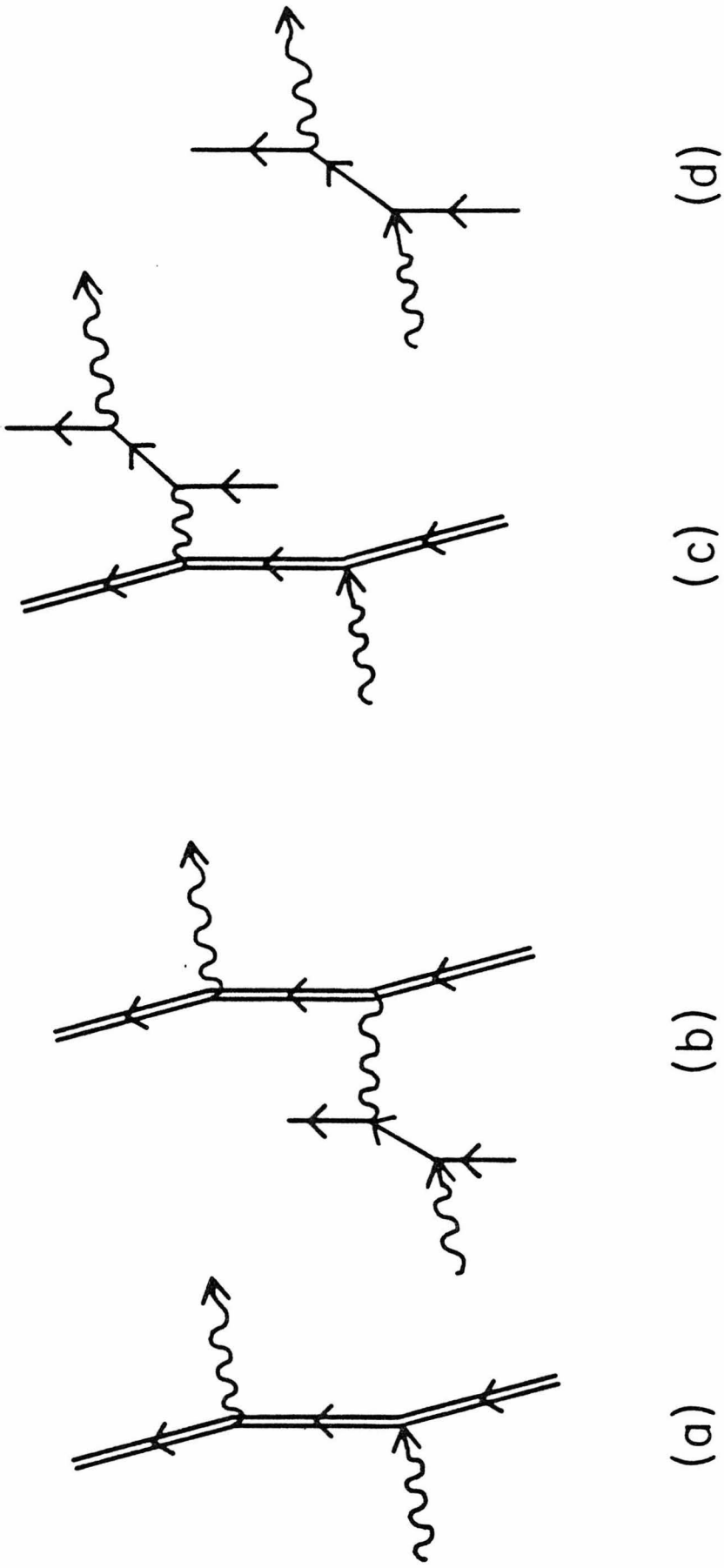

Fig. 2

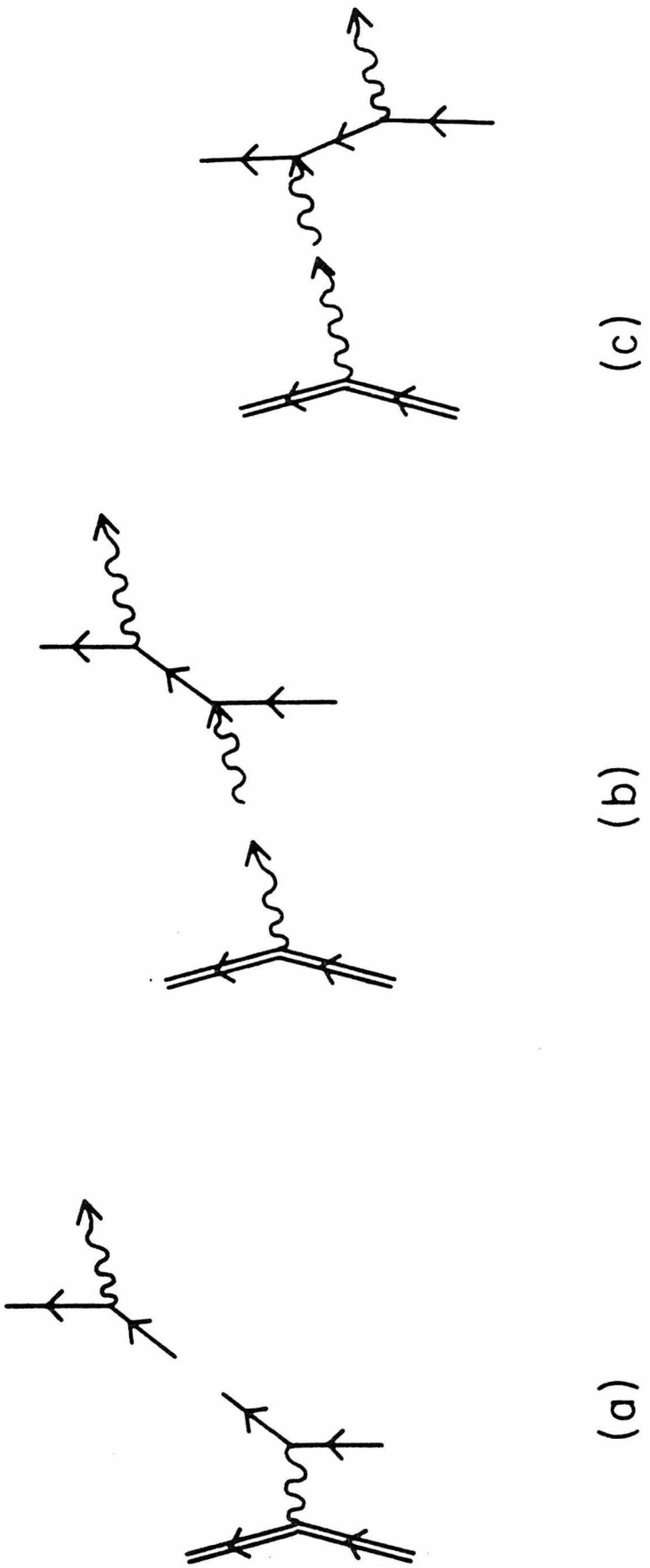

Fig. 3

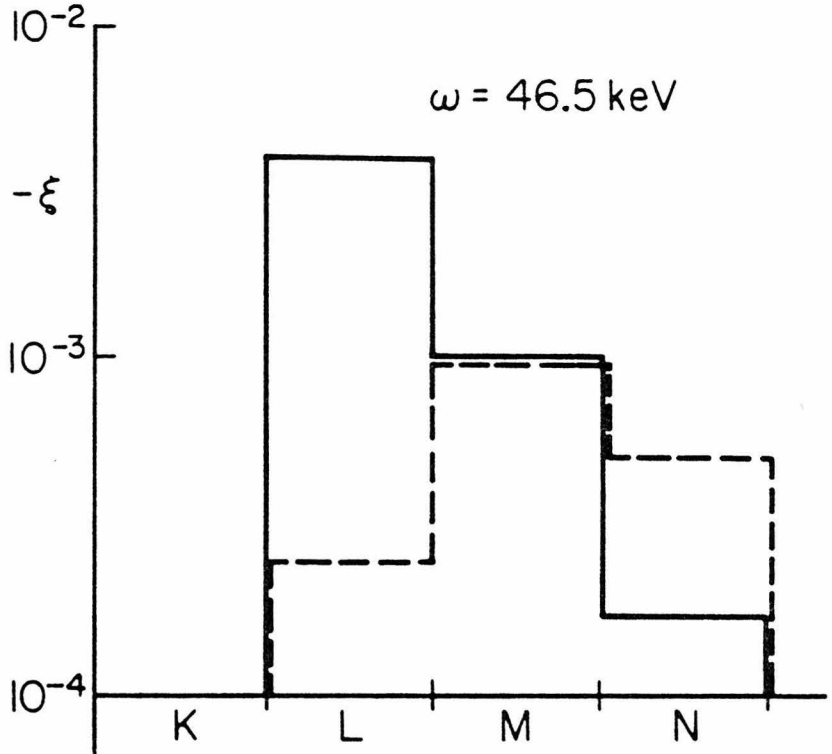
10^{-2}
ω = 46.5 keV
$-\xi$
10^{-3}
10^{-4}
K
L
M
N

Fig. 4a

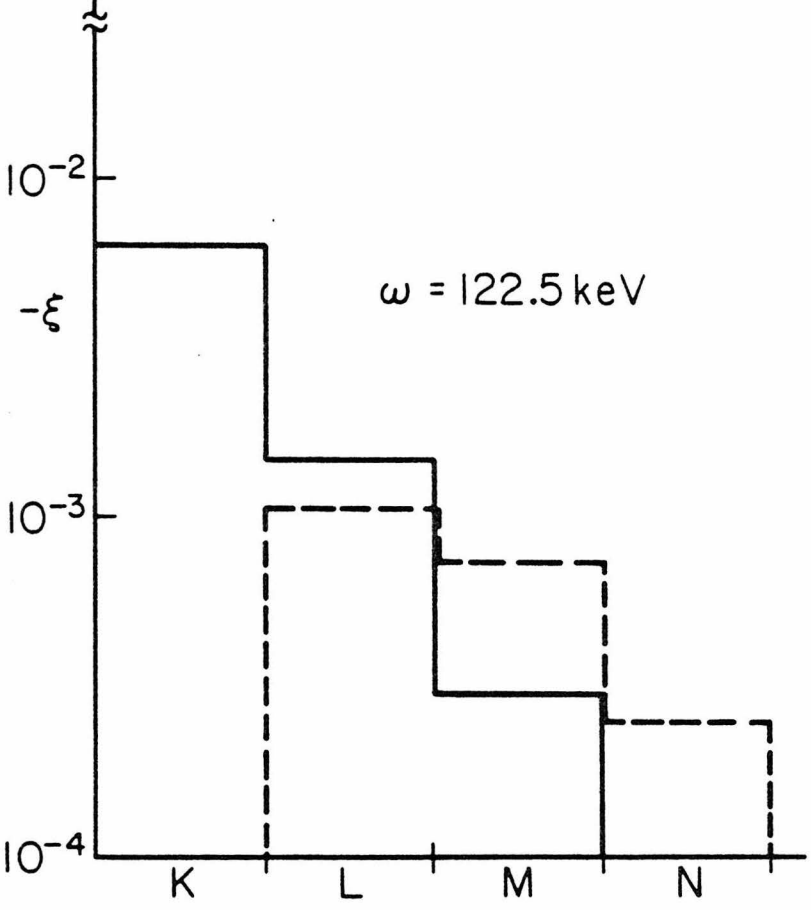
10^{-2}
ω = 122.5 keV
$-\xi$
10^{-3}
10^{-4}
K
L
M
N

Fig. 4b

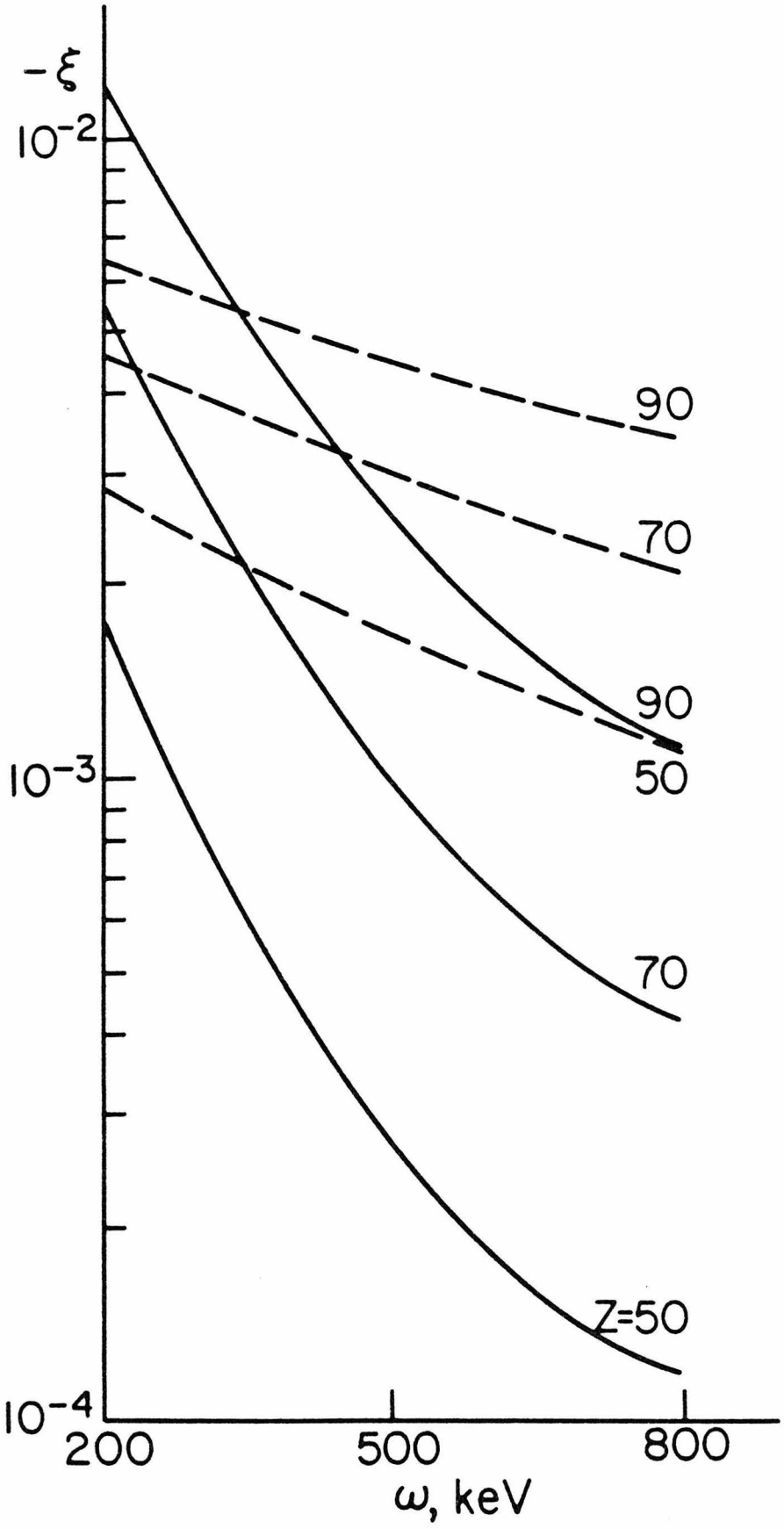

Fig. 5a

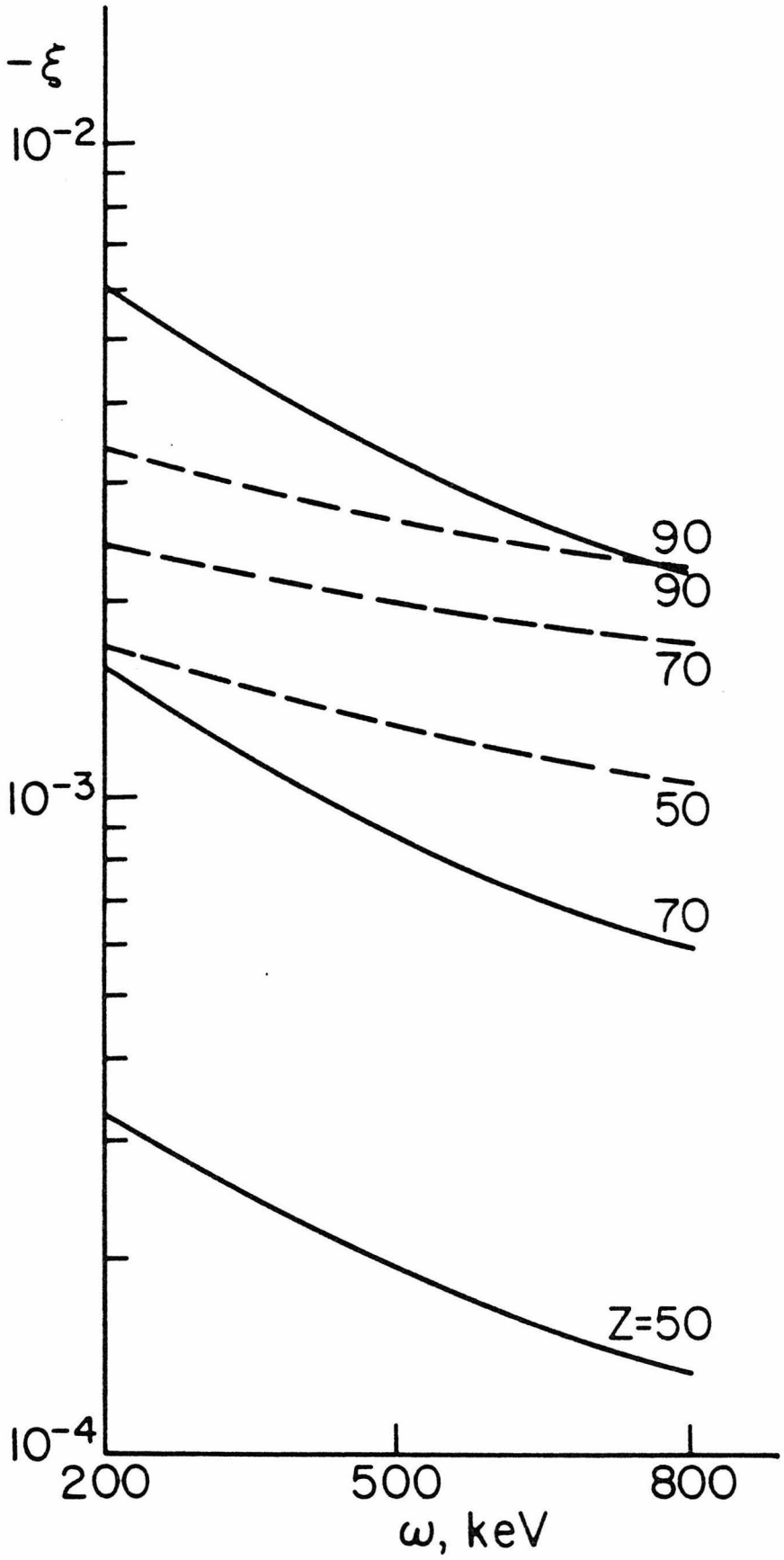

Fig. 5b

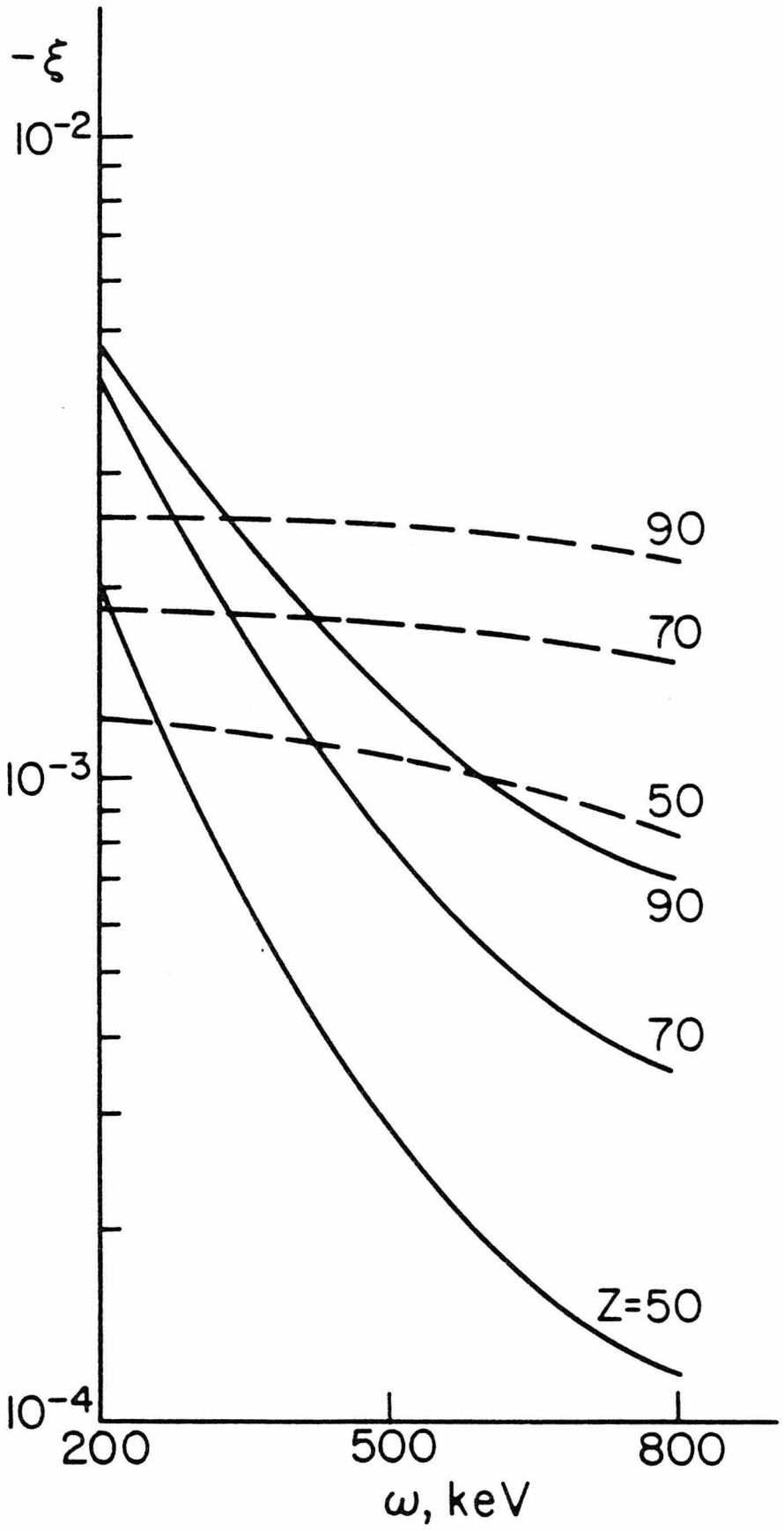

Fig. 5c

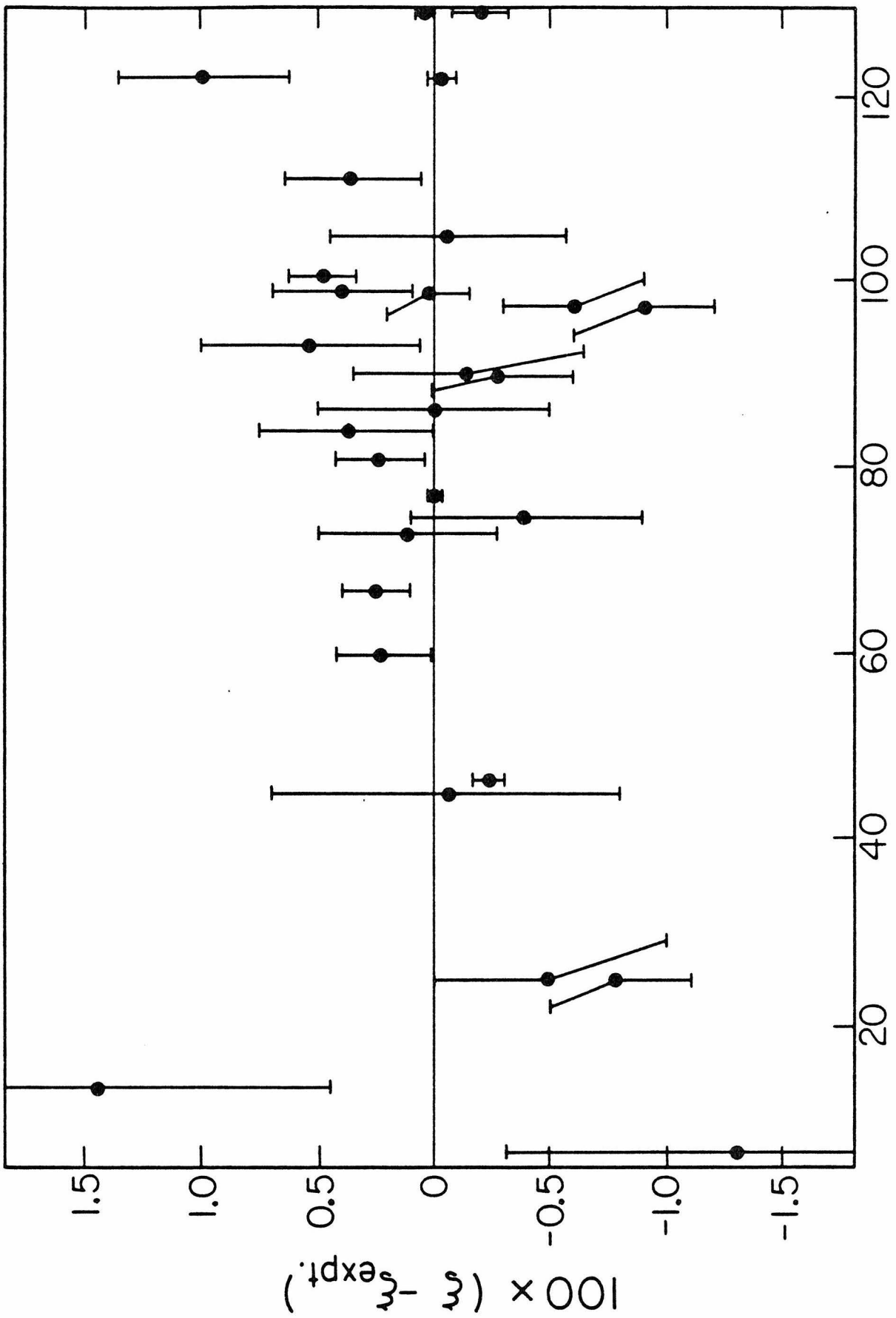

Fig. 6